

## The 4–400 GHz Survey for the 32 Class II Disks in the Taurus Molecular Cloud

CHIA-YING CHUNG <sup>1</sup>, AN-LI TSAI <sup>1</sup>, MELVYN WRIGHT <sup>2</sup>, WENRUI XU <sup>3</sup>, FENG LONG <sup>4</sup>, MARK A. GURWELL <sup>5</sup>, AND  
HAUYU BAOBAB LIU <sup>1,6</sup>

<sup>1</sup>*Department of Physics, National Sun Yat-Sen University, No. 70, Lien-Hai Road, Kaohsiung City 80424, Taiwan, R.O.C.*

<sup>2</sup>*Department of Astronomy, University of California, Berkeley, 501 Campbell Hall, Berkeley, CA 94720-3441, USA*

<sup>3</sup>*Center for Computational Astrophysics, Flatiron Institute, 162 5th Ave, New York, NY10010, USA*

<sup>4</sup>*Lunar and Planetary Laboratory, University of Arizona, Tucson, AZ 85721, USA\**

<sup>5</sup>*Center for Astrophysics | Harvard & Smithsonian, 60 Garden St., Cambridge, MA 02138, USA*

<sup>6</sup>*Center of Astronomy and Gravitation, National Taiwan Normal University, Taipei 116, Taiwan*

### ABSTRACT

We have compiled the  $\sim 4\text{--}400$  GHz broad spectra of 32 Class II protoplanetary disks in the Taurus-Auriga region, which represents the brightest one-third of sources detected in the submillimeter band in this region. The spectra at  $>20$  GHz frequency can be described with a piecewise function: (1) a power law with a spectral index  $\sim 2$  at  $>200$  GHz, (2) a power law with spectral index in the range 0.3–4.2 at 20–50 GHz, and (3) a transition region in between these two power laws which can be characterized by a sigmoid function. This suggests that the flux densities at  $>200$  GHz and  $<50$  GHz are dominated by distinct emission components. At  $>200$  GHz, the emission is likely dominated by the optically thick dust thermal emission in the bulk of the disks. In some sources that were not detected at 6.8 GHz or 10 GHz, embedded high-density dust substructures may contribute to a significant fraction of the flux densities at 30–50 GHz, and the spectral indices are mostly consistent with 2.0. Although, at 30–50 GHz, free-free and/or synchrotron emission may be significant, and some sources in our sample have spectral indices  $< 2.0$ . Based on these results, we hypothesize that high-density dust substructures (e.g., vortices) are often found in resolved Class II protoplanetary disks, and are a precursor to the formation of kilometer-sized planetesimals and rocky planets. They may not present high contrast at  $>200$  GHz frequencies owing to the high optical depth. To probe these dust substructures, high angular resolution observations at  $<100$  GHz are necessary to distinguish them from free-free and synchrotron emission sources. Otherwise, in the analyses of the spatially unresolved spectra, one needs to simultaneously constrain the flux densities of free-free, synchrotron, and dust emission with the observations at  $\sim 5\text{--}50$  GHz.

*Keywords:* Circumstellar dust (236) — Protoplanetary disks (1300) — Pre-main sequence (1289) — Planet formation (1241)

### 1. INTRODUCTION

Dust in protoplanetary disks (PPDs) must be processed to form the ubiquitously detected rocky planets. Initially, the dust grains in PPDs are very small (e.g., in sub- $\mu\text{m}$  sizes) and are well coupled with the gas in the disk. The first step in forming planets is the coagulation of these tiny dust grains into 10–100  $\mu\text{m}$  sized aggregates (for a recent review see Birnstiel 2023). Once formed, these aggregates become dynamically loosely coupled with the bulk of the parent gaseous PPDs due to their small geometric cross-section per unit mass. They tend to migrate inward until they are trapped at a pressure maximum, which may be manifested as the dusty rings that were ubiquitously resolved in the ALMA observations (e.g., Andrews et al. 2018; Long et al. 2018; Francis & van der Marel 2020; Cieza et al. 2021;

Yamaguchi et al. 2024, etc). Owing to the accumulation of a large amount of dust, the recent theoretical and observational studies showed that the dust rings are likely very optically thick (i.e., optical depth  $\tau \gtrsim 3$ ) at  $\gtrsim 100$  GHz frequencies (e.g., Liu et al. 2016; Liu 2019; Carrasco-González et al. 2019; Chung et al. 2024; Delussu et al. 2024). We note that when maximum dust grain size  $a_{\text{max}}$  is comparable or larger than  $\sim 100$   $\mu\text{m}$ , the effective dust scattering opacity may outweigh the dust absorption opacity (Birnstiel et al. 2018). In this case, brightness temperature of dust thermal emission will be lower than dust temperature. The analyses that do not self-consistently consider the effect of dust scattering may misinterpret the observations as optically thin dust emission, potentially leading to underestimates of dust optical depths by an order of magnitude (Liu 2019; Zhu et al. 2019).

\* NASA Hubble Fellowship Program Sagan Fellow

**Table 1.** New JVLA observations (Project code: 22B-033; PI: C.-Y. Chung)

Date (UTC)	Band	Frequency (GHz)	uv-range (k $\lambda$ )	Observed sources	Flux Calib.	Passband Calib.	Gain Calib.
2022 09 30	X	8.0–12.0	1.1–134	DE Tau, CW Tau, Haro 6-39	3C147	3C84	J0403+2600, J0443+3411
2022 10 15	Ka	29.0–37.0	5.2–350	DE Tau, BP Tau, CW Tau, Haro 6-39	3C147	3C84	J0403+2600, J0438+3004
2022 11 02	Ka	29.0–37.0	3.9–370	DE Tau, BP Tau, CW Tau, Haro 6-39	3C147	3C84	J0403+2600, J0438+3004
2022 10 12	Q	40.0–48.0	4.0–450	DE Tau, BP Tau, CW Tau, Haro 6-39	3C147	3C84	J0403+2600, J0438+3004
2022 10 03	X	8.0–12.0	0.7–108	IP Tau	3C147	3C84	J0403+2600
2022 10 01	Ka	29.2–36.9	2.8–384	IP Tau	3C147	3C84	J0403+2600
2022 10 11	Ka	29.0–37.0	6.7–350	IP Tau	3C147	3C84	J0403+2600
2022 11 13	Q	40.0–48.0	5.9–525	IP Tau	3C147	3C84	J0403+2600
2022 11 18	Q	40.1–48.0	5.3–490	IP Tau	3C147	3C84	J0403+2600
2022 10 02	X	8.0–12.0	0.8–119	BP Tau, DS Tau, V836 Tau	3C147	3C84	J0403+2600, J0443+3441
2022 11 08	Ka	29.0–37.0	4.1–390	DS Tau, V836 Tau	3C147	3C84	J0438+3004, J0431+2037
2022 11 13	Ka	29.0–37.0	3.5–390	DS Tau, V836 Tau	3C147	3C84	J0438+3004, J0431+2037
2022 10 02	Q	40.2–47.4	0.5–507	DS Tau, V836 Tau	3C147	3C84	J0438+3004, J0431+2037
2022 10 03	X	8.0–12.0	1.1–134	SU Aur	3C147	3C84	J0443+3441
2022 10 03	Ka	29.2–36.9	3.1–377	SU Aur	3C147	3C84	J0438+3004
2022 10 30	Ka	29.2–36.8	3.7–380	SU Aur	3C147	3C84	J0438+3004
2022 10 13	Q	40.0–48.0	5.5–500	SU Aur	3C147	3C84	J0438+3004
2022 11 07	Q	40.0–48.0	4.3–480	SU Aur	3C147	3C84	J0438+3004
2022 09 30	X	8.0–12.0	0.9–126	(23 targets)*	3C147	3C84	J0403+2600, J0431+2037, J0443+3441

All observations were taken in the C array configuration.

\* These 23 targets are: CY Tau, V892 Tau, RY Tau, FT Tau, IQ Tau, UZ Tau, DL Tau, AA Tau, DN Tau, CI Tau, T Tau, UX Tau, V710 Tau, DM Tau, LkCa 15, DO Tau, GO Tau, DQ Tau, Haro 6-37, DR Tau, UY Aur, GM Aur, AB Aur.

In the rings where there are azimuthally asymmetric pressure maxima, such as the vortices induced by Rossby wave instability or planet-disk interactions, the aggregates will migrate towards the vortices and form dusty crescents or clumps (e.g., the numerical simulations presented in Li et al. 2020; Wu 2024, and references therein). When such localized dust substructures reach high dust-to-gas ratios ( $>0.1$ ), a dynamic instability, namely streaming instability (Youdin & Goodman 2005), can be activated to efficiently collect aggregates into high-density concentrations. It is likely that pebbles or kilometer-sized planetesimals form in these high-density concentrations. Therefore, detecting these high-density dust substructures and determining their masses ( $M_{\text{dust}}$ ) and maximum dust grain sizes ( $a_{\text{max}}$ ) are crucial to understand the formation of rocky planets or solid cores of gas giants. In particular,  $M_{\text{dust}}$  and  $a_{\text{max}}$  can only be reliably estimated by observations in the optically thin regime, where flux density is proportional to optical depth, and the frequency variation of dust absorption opacity can be inferred from the measurements of spectral indices. Observations at optically thinner wavelengths (e.g.  $\lesssim 100$  GHz in frequency) are therefore an outstanding science case for the Karl G. Jansky Very Large Array (JVLA), ALMA

Band 1 (e.g., Di Francesco et al. 2013), the next generation Very Large Array (e.g., van der Marel et al. 2018) and Square Kilometer Array (e.g., Wu et al. 2024) in the future.

Observationally, a spatially resolved example of this scenario is the large transitional disk DM Tau: the previous ALMA 225 GHz observations revealed a bright and optically thick ring at the inner rim of the bulk of the transitional disk (Hashimoto et al. 2021); with lower optical depths, the JVLA Q band (44 GHz;  $\sim 6.8$  mm) observations further detected multiple localized dust clumps in the ring (Liu et al. 2024b; Wu 2024). Fitting the spectrum indicated that  $a_{\text{max}}$  is  $\sim 50$   $\mu\text{m}$  in the bulk of the DM Tau disk, while in the localized dust clumps the lower limit of  $a_{\text{max}}$  is 300  $\mu\text{m}$  (Liu et al. 2024b). This is consistent with promoted grain growth in the localized dust substructures. Another similar example is the transitional disk LkCa 15 (Isella et al. 2014). Recent observations found lopsided distributions of (grown) dust embedded in a few more disks (e.g., PDS 70: Liu et al. 2024a; Doi et al. 2024; LkCa 15: Long et al. 2022; MWC 758: Casassus et al. 2019; CIDA1: Hashimoto et al. 2023; WL 17: Han et al. 2023, etc), which may signify planet-disk interactions or the presence of vortices (e.g., Li et al. 2020; Wu 2024).

**Table 2.** Archival Disk@EVL A observations (Project code: AC982; PI: C. Chandler)

Date (UTC)	Band	Frequency (GHz)	Array Config.	uv-range (k $\lambda$ )	Observed sources	Flux Calib.	Passband Calib.	Gain Calib.
2010 07 11	C	4.8–6.8	D	0.5–21.5	MHO 1/2, CY Tau, V892 Tau, RY Tau, IQ Tau GO Tau, DO Tau, DL Tau, UZ Tau, FT Tau, AA Tau, DN Tau, CI Tau, LkCa 15 T Tau, UX Tau, V710 Tau, Haro 6-37, DR Tau, DM Tau, DQ Tau GM Aur, AB Aur, UY Aur	3C147	3C84	J0403+2600 J0431+2037 J0443+3441
2010 08 23	K	20.0–22.0	D	1.8–73	MHO 1/2, CY Tau, V892 Tau, RY Tau GO Tau, DO Tau, DL Tau, UZ Tau, IQ Tau, FT Tau AA Tau, DN Tau, CI Tau, LkCa 15, T Tau	3C147	3C84	J0403+2600 J0431+2037
2010 08 24	K	20.0–22.0	D	1.8–72	UX Tau, V710 Tau, DM Tau, Haro 6-37, DQ Tau, DR Tau GM Aur, AB Aur, UY Aur	3C147	3C84	J0431+2037 J0443+3441
2010 08 20	Ka	31.7–33.6	D	3.6–107	MHO 1/2, CY Tau, V892 Tau, RY Tau GO Tau, DO Tau, DL Tau, UZ Tau, FT Tau, IQ Tau DN Tau, AA Tau, CI Tau, LkCa 15, T Tau	3C147	3C84	J0403+2600 J0431+2037
2010 08 21	Ka	31.7–33.6	D	3.3–98	UX Tau, V710 Tau, DM Tau, Haro 6-37, DQ Tau, DR Tau GM Aur, AB Aur, UY Aur	3C147	3C84	J0431+2037 J0443+3441
2010 09 12	Ka	31.7–33.6	D	4.1–114	CY Tau DO Tau, DL Tau, UZ Tau, IQ Tau, AA Tau FT Tau, DN Tau, CI Tau, DM Tau	3C147	3C84	J0403+2600 J0431+2037
<sup>a</sup> 2010 08 10	Q	41.0–43.0	D	–	MHO 1/2, CY Tau, V892 Tau, RY Tau GO Tau, DO Tau, DL Tau, UZ Tau, IQ Tau, FT Tau AA Tau, DN Tau, CI Tau, LkCa 15	3C147	3C84	J0403+2600 J0431+2037
2010 08 10	Q	41.0–43.0	D	5.5–145	GM Aur, AB Aur, UY Aur T Tau, UX Tau, V710 Tau, DM Tau, Haro 6-37, DQ Tau, DR Tau	3C147	3C84	J0443+3441 J0431+2037
2010 08 11	Q	41.0–43.0	D	4.6–137	MHO 1/2, CY Tau, V892 Tau, RY Tau GO Tau, DO Tau, DL Tau, UZ Tau, IQ Tau, FT Tau AA Tau, DN Tau, CI Tau, LkCa 15	3C147	3C84	J0403+2600 J0431+2037
2010 08 12	Q	41.0–43.0	D	4.2–134	T Tau, UX Tau, V710 Tau, DM Tau, Haro 6-37, DQ Tau, DR Tau GM Aur, AB Aur, UY Aur	3C147	3C84	J0431+2037 J0443+3441
2010 10 28	Q	41.0–43.0	C	11.3–450	MHO 1/2, CY Tau, V892 Tau, RY Tau GO Tau, DO Tau, DL Tau, UZ Tau, IQ Tau, FT Tau AA Tau, DN Tau, CI Tau, LkCa 15	3C147	3C84	J0403+2600 J0431+2037
2010 08 30	Q	41.0–43.0	D	4.1–114	CY Tau GO Tau, DO Tau, DL Tau, UZ Tau, IQ Tau, FT Tau AA Tau, DN Tau, CI Tau, LkCa 15, V710 Tau, DM Tau, Haro 6-37, DR Tau	3C147	3C84	J0403+2600 J0431+2037

**Table 2** *continued*

Table 2 (continued)

Date (UTC)	Band	Frequency (GHz)	Array Config.	uv-range (k $\lambda$ )	Observed sources	Flux Calib.	Passband Calib.	Gain Calib.
2010 09 11	K	20.0–22.0	D	2.2–74	V710 Tau, DM Tau, Haro 6-37, DR Tau	3C147	3C84	J0431+2037
<sup>a</sup> 2010 09 10	Ka	31.7–33.6	D	–	GM Aur, AB Aur	3C147	3C84	J0443+3441
<sup>a</sup> 2010 09 13	Ka	31.7–33.6	D	–	GM Aur, AB Aur	3C147	3C84	J0443+3441
2010 11 01	Ka	30.0–38.0	C	7.6–422	GM Aur T Tau, DQ Tau UY Aur	3C147	3C84	J0431+2037 J0443+3441
2010 11 13	Ka	30.0–38.0	C	8.0–427	DL Tau	3C147	3C84	J0431+2037
2010 11 14	Ka	30.0–38.0	C	8.0–349	GM Aur	3C147	3C84	J0443+3441
2012 03 06	Ka	30.0–38.0	C	7.9–415	GM Aur	3C147	3C84	J0439+3045
2010 09 02	Q	41.0–43.0	D	4.5–127	GM Aur, AB Aur	3C147	3C84	J0443+3441
2010 11 13	Q	41.0–43.0	C	8.0–441	CY Tau	3C147	3C84	J0403+2600
2010 11 15	Q	41.0–43.0	C	8.8–457	DN Tau	3C147	3C84	J0431+2037
2010 11 28	Q	41.0–43.0	C	4.3–454	DR Tau	3C147	3C84	J0431+2037
2010 11 23	Q	41.0–43.0	C	6.1–457	UX Tau	3C147	3C84	J0431+2037
2010 11 19	Q	41.0–43.0	C	5.6–445	AB Aur	3C147	3C84	J0443+3441
2010 12 09	Q	41.0–43.0	C	4.3–456	Haro 6-37	3C147	3C84	J0431+2037
2010 12 13	Q	41.0–43.0	C	4.9–456	DM Tau	3C147	3C84	J0431+2037

<sup>a</sup> Calibration failed.

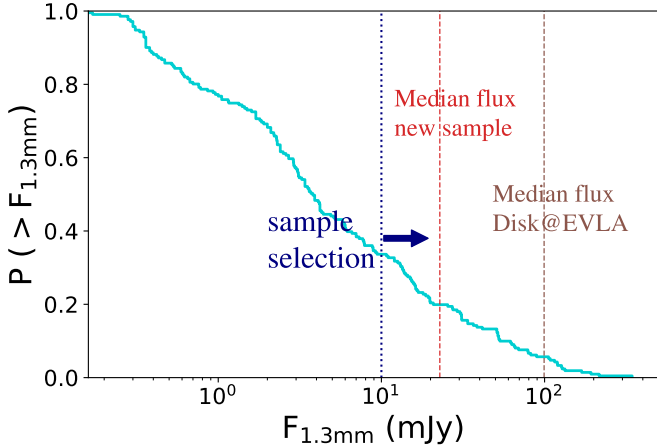


**Figure 1.** The cumulative distribution of  $F_{1.3\text{mm}}$  of 211 Class II disks in Taurus-Auriga region (quoted from [Akeson et al. 2019](#)). The brown and red dashed lines label the median  $F_{1.3\text{mm}}$  of the Disk@EVLA sample and the median  $F_{1.3\text{mm}}$  the new 8 sources sample, respectively. The blue dotted line label the sample selection criterion on flux density.

However, the majority of the Class II PPDs have  $<50$  au dust disk radii at 1.3 mm wavelength (c.f., [Long et al. 2019](#); [Cieza et al. 2019](#); [Cazzoletti et al. 2019](#)). Due to the sensitivity and angular resolution limitations of current observing facilities, we cannot resolve the high-density substructures as clearly as cases like DM Tau, PDS 70, MWC 758, LkCa 15, and CIDA1. To test whether or not the aforementioned physical picture is common for Class II disks, a more practical approach is examining the spectra over a broad frequency range (more below). Observations at shorter wavelengths are sensitive to the emission of small dust particles in the bulk of the PPDs; larger (e.g., mm–cm sized) dust particles emit more efficiently at longer wavelengths. Observations at longer wavelengths (e.g.,  $\nu < 50$  GHz) preferentially traces the grown dust (e.g.,

Out of these, 24 sources that are relatively bright at 1.2 mm wavelength were observed by the Disk@EVLA project (VLA project code: AC982) at C (4.8–6.8 GHz), K (20.0–22.0 GHz), Ka (31.7–33.6 GHz), and Q (41.0–43.0 GHz) bands (more in Section 2.3). We utilized the Disk@EVLA data taken in the D array configuration and C array configuration, which are not subject to missing short-spacing. We also carried out only new X band (8–12 GHz) observations for 23<sup>1</sup> of these 24 sources (see Section 2.2).

According to recent ALMA surveys (e.g., [Akeson et al. 2019](#)), the Disk@EVLA samples are considerably brighter

<sup>1</sup> We missed to select MHO 1/2 due to the different naming convention in SMA ([Chung et al. 2024](#)) and Disk@EVLA surveys. Nevertheless, MHO 1/2 was detected in the C band observations of the Disk@EVLA project, and in the  $<10$  GHz observations of [Dzib et al. \(2015\)](#) (Figure 3).

$a_{\text{max}} > 1$  mm) that is concentrated in the high column density substructures ([Hildebrand 1983](#); [Draine 2006](#)).

In a recent study, [Chung et al. \(2024\)](#) presented a survey of 47 Class II protoplanetary disks (PPDs) in the Taurus-Auriga region, focusing on sources with high 850  $\mu\text{m}$  fluxes (top 32% percentile). They found that the spectral indices in the 200–400 GHz frequency range (hereafter  $\alpha_{200-400\text{GHz}}$ ) for the selected sources were concentrated within an extremely narrow range of  $2.0 \pm 0.2$ , which is consistent with the dust thermal emission in the bulk of the optically thick dust rings. To probe the embedded, high-density (grown) dust substructures in these disks, longer wavelengths observations are demanded to penetrate into the disk mid-planes. However, considering the relatively long observing time required for achieving adequate signal-to-noise ratios at frequencies below 50 GHz, in this work, we focus on the bright sub-sample selected from [Chung et al. \(2024\)](#) and present their  $\sim 4$ –200 GHz spectra.

The target source selections and observations are introduced in Section 2. Details of our data processings are described in Section 3. Specifically, we included the JVLA observations at 4–50 GHz frequencies which were taken through our own project (22B-033; PI: C.-Y. Chung) and through the archival Disk@EVLA observations (AC982; PI: C. Chandler). We also quoted various previous observations in between 4 GHz and 400 GHz. The results are summarized in Section 4. The physical implications of our observations are briefly discussed in Section 5. Our conclusion is given in Section 6. In Appendix A, we characterize the observed spectra with piecewise functions that are independent of specific physical models.

## 2. OBSERVATIONS

### 2.1. Sample selection

We chose to analyze a subset of bright sources from the SMA Taurus-Auriga survey ([Chung et al. 2024](#); Figure 1). A total of 32 Class II objects were selected.

at 1.3 mm band compared to typical Class II disks (see Figure 1). Such a target source selection strategy was likely due to the limited, 2 GHz available continuum bandwidth during the Disk@EVLA observations. We took advantage of the presently available, 8 GHz continuum bandwidth at Ka and Q bands to observe another 8 objects that are fainter at 1.2 mm wavelength (Figure 1). When selecting these 8 sources, we (i) required their flux densities at 1.3 mm wavelength ( $F_{1.3\text{mm}}$ ) to be larger than 10 mJy to ensure a  $\gtrsim 5$ - $\sigma$  significance in every 8 GHz bandwidth in our new Ka and Q band observations (see Section 2.2), and (ii) avoided the known binary or multiple system.

### 2.2. New JVLA observations (JVLA/22B-033)

We carried out new JVLA X band (8.0–12.0 GHz) observations for 31 of the 32 selected sources (Section 2.1). In addition, we carried out Ka (29.0–37.0 GHz) and Q (40.0–48.0 GHz) observations for the 8 objects that were not previously observed by the Disk@EVLA project. Our JVLA

**Table 3.** Imaging profiles

Source	RA	Dec	$\theta_{6.8\text{ GHz}}$	$\theta_{10.0\text{ GHz}}$	$\theta_{21.0\text{ GHz}}$	$\theta_{33.0\text{ GHz}}$	$\theta_{44.0\text{ GHz}}$	$\sigma_{6.8\text{ GHz}}$	$\sigma_{10.0\text{ GHz}}$	$\sigma_{21.0\text{ GHz}}$	$\sigma_{33.0\text{ GHz}}$	$\sigma_{44.0\text{ GHz}}$
	(hh:mm:ss)	(dd°mm'ss'')	(")	(")	(")	(")	(")	(mJy)	(mJy)	(mJy)	(mJy)	(mJy)
AA Tau	04:34:55.43	24°28'52''70	15.4 × 13.8	2.9 × 2.4	4.5 × 3.5	2.9 × 2.2	2.7 × 1.7	0.012	0.034	0.06	0.03	0.10
AB Aur	04:55:45.85	30°33'03''91	15.9 × 14.1	3.0 × 2.4	3.7 × 3.4	2.8 × 2.4	1.0 × 0.6	0.030	0.033	0.03	0.05	0.03
BP Tau	04:19:15.84	29°06'26''51	–	3.2 × 2.5	–	1.0 × 0.7	1.0 × 0.6	–	0.025	–	0.02	0.11
CI Tau	04:33:52.02	22°50'29''82	15.3 × 13.2	3.2 × 2.6	4.3 × 3.4	3.1 × 2.2	1.9 × 1.4	0.012	0.036	0.05	0.06	0.16
CW Tau	04:14:17.01	28°10'57''38	–	2.4 × 2.3	–	1.2 × 0.7	1.2 × 0.6	–	0.029	–	0.04	0.13
CY Tau	04:17:33.74	28°20'46''40	18.8 × 14.7	3.0 × 2.4	5.7 × 3.5	2.9 × 2.6	0.9 × 0.6	0.055	0.048	0.10	0.08	0.03
DE Tau	04:21:55.65	27°55'05''75	–	2.5 × 2.3	–	1.1 × 0.7	1.0 × 0.6	–	0.011	–	0.02	0.08
DL Tau	04:33:39.09	25°20'37''81	16.1 × 14.4	3.1 × 2.5	5.5 × 3.5	0.7 × 0.7	2.6 × 1.8	0.027	0.040	0.11	0.02	0.19
DM Tau	04:33:48.75	18°10'09''68	15.4 × 13.9	3.3 × 2.4	4.2 × 3.6	2.9 × 2.1	0.9 × 0.7	0.013	0.033	0.01	0.03	0.02
DN Tau	04:35:27.38	24°14'58''58	15.6 × 13.6	3.1 × 2.6	4.3 × 3.4	2.9 × 2.4	0.7 × 0.6	0.015	0.034	0.07	0.07	0.03
DO Tau	04:38:28.60	26°10'49''13	17.9 × 14.4	3.0 × 2.4	5.6 × 3.5	3.1 × 2.7	2.3 × 1.5	0.043	0.035	0.15	0.10	0.16
DQ Tau	04:46:53.06	16°59'59''92	15.8 × 14.0	3.2 × 2.4	4.1 × 3.4	1.6 × 0.9	2.3 × 1.8	0.037	0.032	0.04	0.55	0.11
DR Tau	04:47:06.22	16°58'42''59	15.3 × 13.2	3.2 × 2.4	3.9 × 3.5	3.1 × 2.4	1.0 × 0.6	0.016	0.034	0.01	0.04	0.03
DS Tau	04:47:48.60	29°25'10''80	–	3.0 × 2.5	–	1.1 × 0.7	0.6 × 0.5	–	0.015	–	0.01	0.05
FT Tau	04:23:39.20	24°56'13''90	15.9 × 14.1	3.1 × 2.5	5.7 × 3.3	2.8 × 2.1	2.2 × 1.7	0.025	0.035	0.14	0.11	0.12
GM Aur	04:55:10.99	30°21'58''99	15.4 × 14.1	3.0 × 2.4	3.8 × 3.4	0.9 × 0.8	2.6 × 1.9	0.021	0.035	0.01	0.01	0.11
GO Tau	04:43:03.08	25°20'18''39	16.6 × 14.4	3.0 × 2.4	6.0 × 3.5	3.4 × 2.8	2.6 × 1.7	0.018	0.035	0.06	0.08	0.11
Haro 6-37	04:46:59.09	17°02'39''73	15.6 × 13.0	3.2 × 2.4	4.2 × 3.5	3.1 × 2.5	1.2 × 0.9	0.074	0.024	0.02	0.04	0.03
Haro 6-39	04:52:09.71	30°37'45''02	–	2.4 × 2.2	–	1.2 × 0.7	1.0 × 0.6	–	0.008	–	0.02	0.09
IP Tau	04:24:57.09	27°11'56''12	–	3.9 × 2.6	–	1.3 × 0.8	0.7 × 0.6	–	0.010	–	0.01	0.04
IQ Tau	04:29:51.56	26°06'44''52	19.7 × 15.1	3.0 × 2.5	5.0 × 3.5	3.1 × 2.3	2.5 × 1.7	0.022	0.033	0.05	0.03	0.09
LkCa 15	04:39:17.80	22°21'03''11	15.0 × 12.0	3.1 × 2.4	3.9 × 3.4	3.0 × 2.3	2.4 × 1.8	0.008	0.034	0.03	0.05	0.13
MHO 1/2	04:14:26.28	28°06'02''85	18.9 × 14.8	–	5.7 × 3.5	2.9 × 2.7	2.1 × 1.4	0.026	–	0.14	0.15	0.18
RY Tau	04:21:57.42	28°26'35''12	19.4 × 15.2	3.0 × 2.4	5.5 × 3.5	2.9 × 2.7	2.1 × 1.5	0.041	0.035	0.15	0.15	0.17
SU Aur	04:55:59.39	30°34'01''11	–	2.5 × 2.2	–	0.9 × 0.7	0.7 × 0.6	–	0.012	–	0.01	0.03
T Tau	04:21:59.45	19°32'06''20	16.5 × 11.8	3.2 × 2.4	3.8 × 3.3	1.8 × 1.1	2.3 × 1.8	0.026	0.039	0.22	0.14	0.29
UX Tau	04:30:04.01	18°13'49''19	15.5 × 12.0	3.2 × 2.4	6.7 × 3.4	3.3 × 2.8	1.2 × 0.8	0.015	0.026	0.04	0.04	0.03
UY Aur	04:51:47.40	30°47'13''14	17.2 × 14.2	3.0 × 2.4	3.6 × 3.4	1.3 × 0.9	2.3 × 1.8	0.028	0.011	0.05	0.02	0.12
UZ Tau	04:32:43.08	25°52'30''66	17.4 × 14.2	2.9 × 2.4	5.4 × 3.5	3.2 × 2.7	1.9 × 1.3	0.029	0.034	0.13	0.11	0.20
V710 Tau	04:31:57.81	18°21'37''67	15.4 × 12.4	3.2 × 2.4	4.8 × 3.5	3.1 × 2.7	2.3 × 1.8	0.009	0.023	0.02	0.03	0.08
V836 Tau	05:03:06.60	25°23'19''33	–	3.1 × 2.5	–	1.0 × 0.7	0.6 × 0.5	–	0.082	–	0.02	0.11
V892 Tau	04:18:40.62	28°19'15''16	18.6 × 14.8	3.1 × 2.5	5.7 × 3.5	2.9 × 2.7	2.1 × 1.5	0.032	0.039	0.18	0.15	0.18

NOTE— Column 1: Source name. Column 2, 3: J2000 coordinates. Column 4, 5, 6, 7, 8: FWHM of the synthesized beam of the C band (6.8 GHz), X band (10.0 GHz), K band (21.0 GHz), Ka band (33.0 GHz) and Q band (44.0 GHz) observations. Column 9, 10, 11, 12, 13: The achieved rms noise of the C band, X band, K band, Ka band and Q band observations.

observations took place between September and November 2022, with observing details summarized in Table 1.

We employed the standard 3-bit continuum setups for the Q, Ka, and X bands observations. In Q and Ka band observations, we employed the WIDAR correlator that was configured with four baseband pairs observing dual polarization; each baseband covers a 2 GHz intermediate frequency (IF) range, and the four basebands were tuned to separated frequencies to provide 8 GHz aggregate bandwidth. In X band observations, the WIDAR correlator was configured with two baseband pairs with the IF coverages to provide 4 GHz aggregate bandwidth for dual polarization.

The observations were conducted in the C array configuration. In these new JVLA observations, the achieved

synthesized beam full width at half maxima (FWHM) are 0''71 ( $\sim 99.4$  AU), 0''95 ( $\sim 133$  AU), 3''14 ( $\sim 440$  AU) at Q, Ka, and X bands, respectively. Our observations are not affected by missing short-spacing as the known disk sizes fall well within the maximum recoverable scale provided by the  $uv$  coverage (Table 1).

For each target source, we estimated their flux densities at Ka and Q bands based on their  $F_{1.3\text{ mm}}$  (Chung et al. 2024) and assuming a spectral index of  $\alpha = 3.5$ . We then accordingly allocated on-source integration time such that each target source can be detected at Ka and Q bands at  $\gtrsim 5$ - $\sigma$  significances in 8 GHz aggregated bandwidth. We allocated the X band on-source integration time such that the X band observations can achieve the same root-mean-square (RMS) noise levels as the Ka band observations. The RMS noises

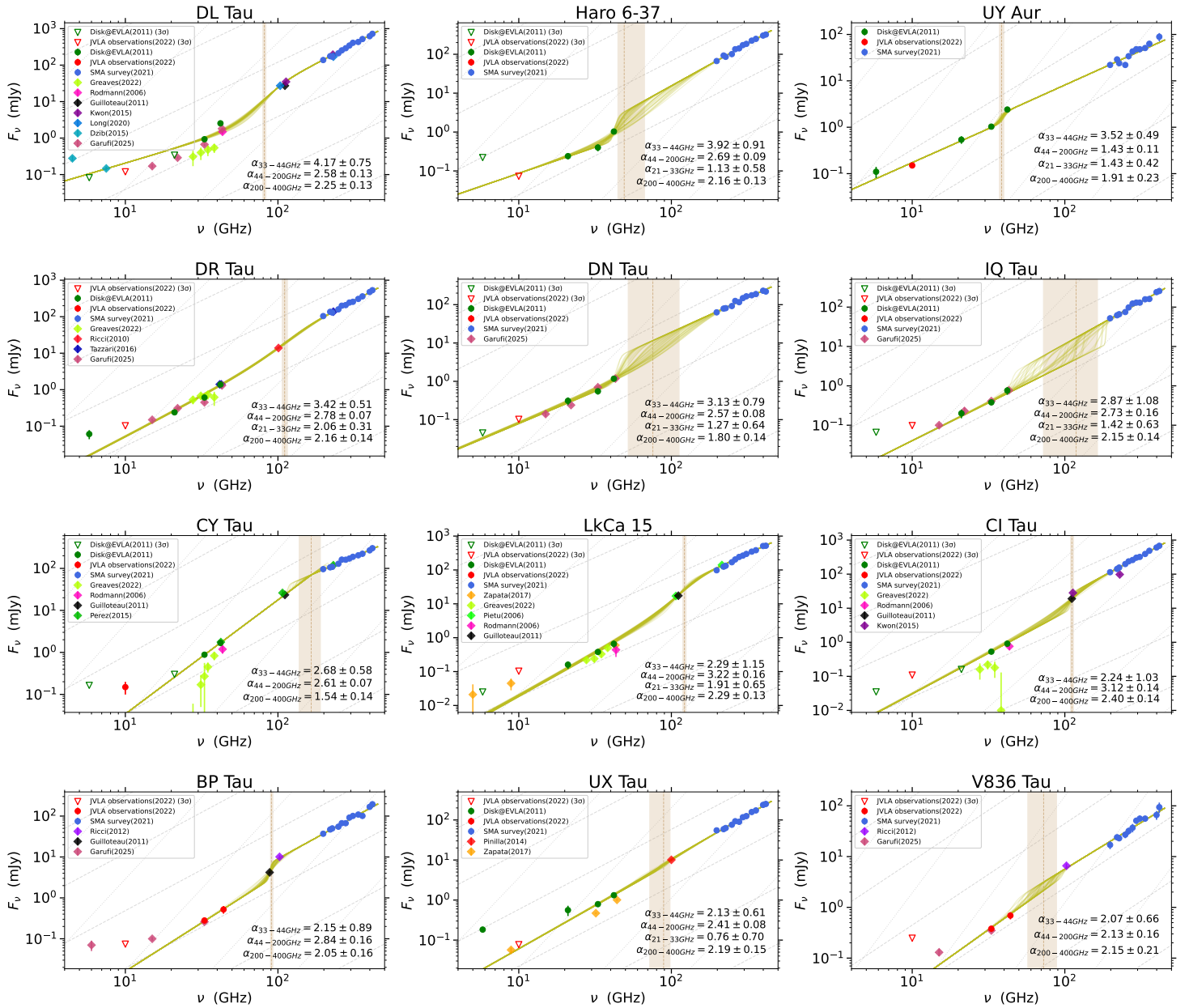


**Figure 2.** The 4–400 GHz spectra of our sample of 32 Class II protoplanetary disks in the Taurus-Auriga region. The flux densities in the Disk@EVLA observations (Section 2.3), the SMA survey (Chung et al. 2024), and the new JVA observations (Section 2.2) are shown by the green, blue and red filled points, respectively. The  $3\text{-}\sigma$  upper limit of flux densities in the Disk@EVLA and the new JVA observations are shown by green and red inverted triangles. We compiled and quoted some flux densities measurements published over 2004–2025 (Acke et al. 2004; Piétu et al. 2006; Rodmann et al. 2006; Ricci et al. 2010; Guilloteau et al. 2011; Ricci et al. 2012; Pinilla et al. 2014; Rodríguez et al. 2014; Dzib et al. 2015; Pérez et al. 2015; Tazzari et al. 2016; Zapata et al. 2017; Tripathi et al. 2018; Huang et al. 2020; Long et al. 2020; Greaves & Mason 2022; Ueda et al. 2022; Garufi et al. 2025). The 32 sources are arranged in the descending order of  $\alpha_{33-44\text{GHz}}$ . The  $\alpha_{33-44\text{GHz}}$ ,  $\alpha_{44-200\text{GHz}}$  and  $\alpha_{21-33\text{GHz}}$  were calculated between two adjacent bands and shown in the lower right of each panel; the  $\alpha_{200-400\text{GHz}}$  was quoted from Chung et al. (2024). The olive semitransparent lines are 50 random draws of the fitting parameters extracted from the MCMC samplings. The best fit value of the parameter  $b/\omega$  (Appendix A), with its uncertainty, are shown by the brown vertical line and shaded area. The spectra are overlaid with the gray dashed and dotted lines, which indicate the spectral indices of  $\alpha = 2.0$  and  $\alpha = 4.0$ , respectively.

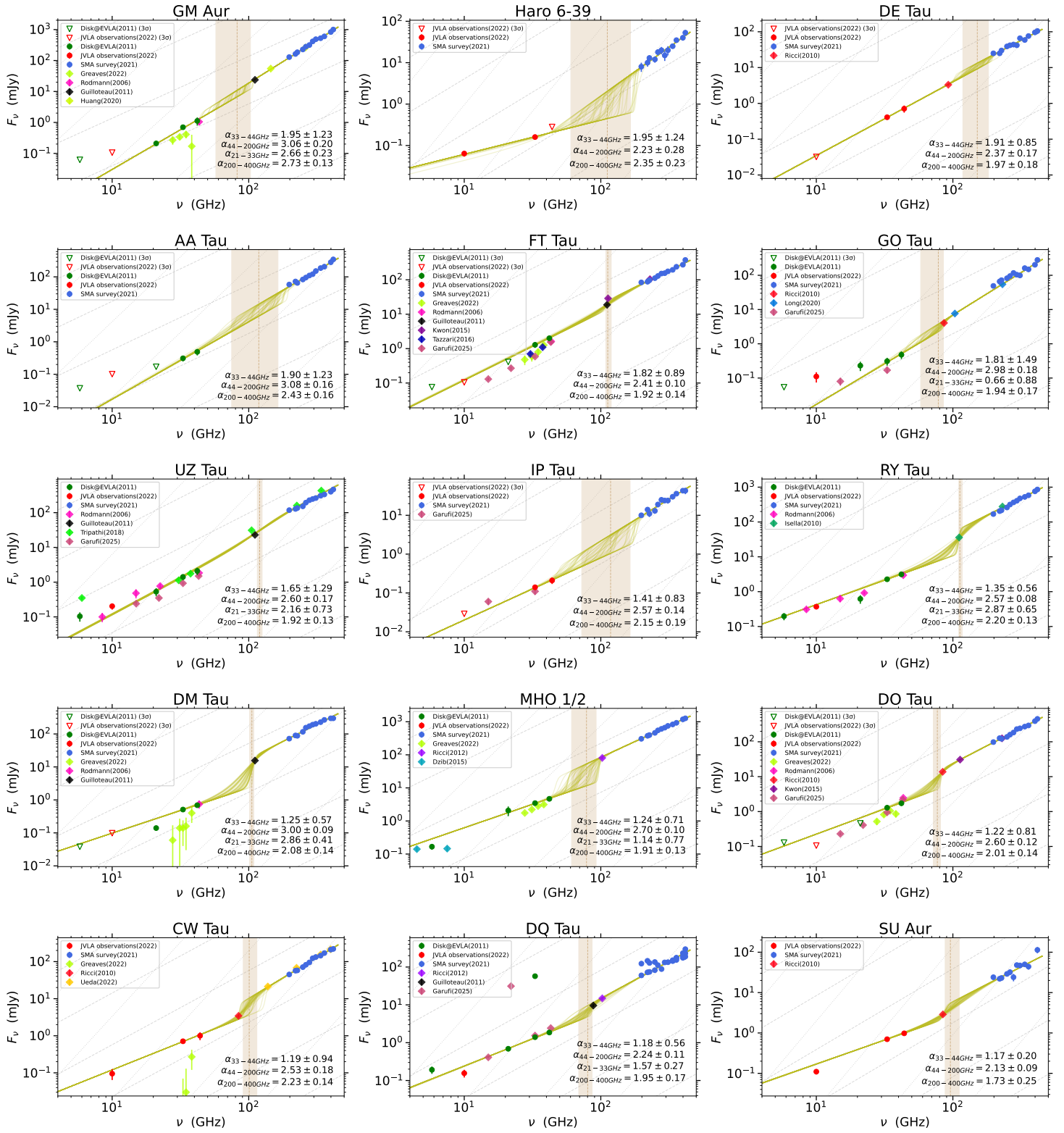


Figure 3. Continuation of Figure 2.

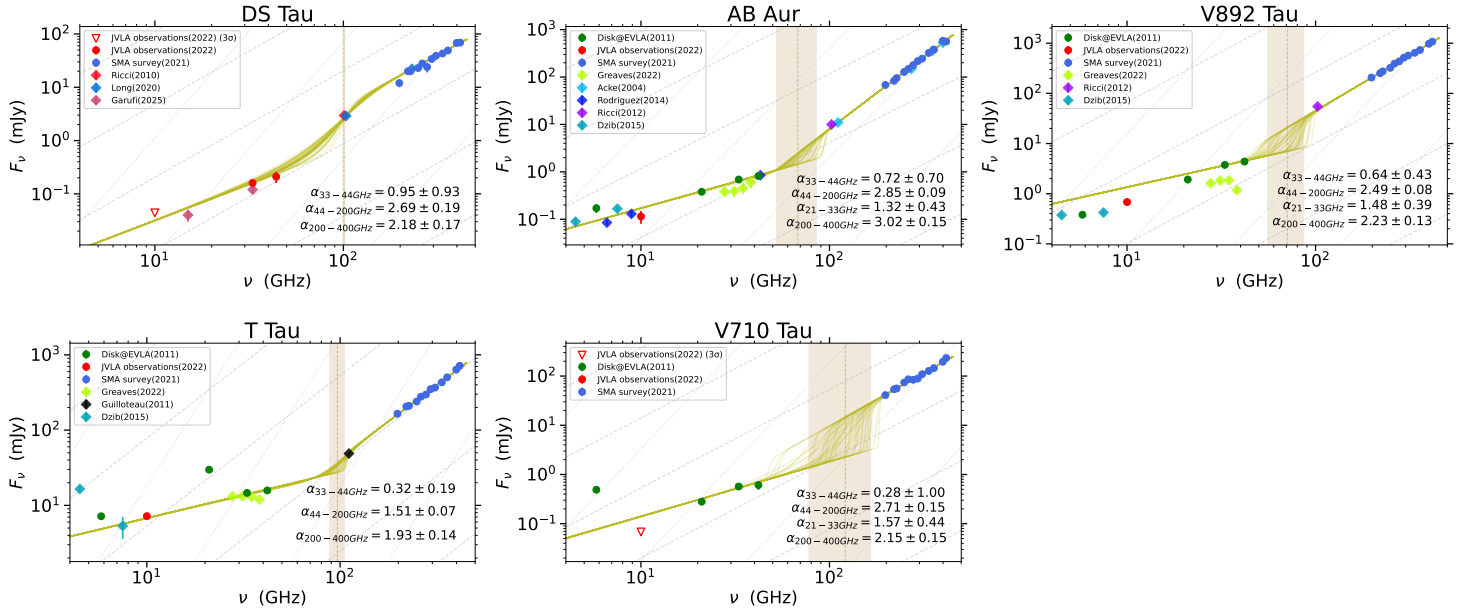


Figure 4. Continuation of Figure 2.

of our X band observations can discern the confusion of optically thin free-free emission, which has been typically assumed to have spectral indices  $\alpha \sim 0$ . This assumption is not necessarily realistic, which is discussed in Section 4.3. For the observations on all sources and at all frequency bands, we adopted a minimum on-source time of 48 seconds in case of temporary technical issues during the observations.

We observed the quasar, 3C84, at the beginning of each track of observations for passband calibrations. We observed the quasar, 3C147, at the end of each track of observations for absolute flux calibrations. For the Q, Ka, and X bands observations, we quoted the nominal absolute flux uncertainties of 10%, 10%, and 5%, respectively. We selected the complex gain calibrators based on the flux densities, and the angular separations from our selected target sources. We adopted the officially recommended calibration cycle times for the C array configuration, which are 4 mins, 5 mins, and 10 mins at Q, Ka, and X bands, respectively.

### 2.3. Archival Disk@EVLA observations (AC982)

We retrieved the archival JVLA Q (41.0–43.0 GHz), Ka (31.7–33.6 GHz), K (20.0–22.0 GHz) and C (4.8–6.8 GHz) band observations that were taken with the Disk@EVLA project (PI: C. Chandler). These observations were taken in 2010, from July to December, in the C and D array configurations. The observational setup, observed sources, and adopted calibrators are listed in Table 2. The Ka band observations on 2010 September 10 (execution block ID: eb1922677) cannot be calibrated due to poor data quality; The Ka band observations on 2010 September 13 (scheduling block ID: sb1925247\_1) cannot be calibrated because the complex gain calibrators were detected at low signal-to-noise ratios (SNR).

## 3. DATA REDUCTION

### 3.1. Calibration

We manually calibrated our new JVLA observations and the archival data using the Common Astronomy Software Applications (CASA; version 6.4) software package (CASA Team et al. 2022), following the standard calibration procedures. In the initial data inspection, we manually flagged the antennae and spectral windows that have poor response, and flagged the spectral channels that were subject to significant radio frequency interference (RFI). After applying antenna position correction, elevation-dependent gain curve, tropospheric opacity correction and requantizer gain, we bootstrapped delay and passband calibrations. We manually flagged the scans on the gain calibrators that were subject to poor phase coherence, as well as the associated scan on the science target sources, before performing complex gain calibrations. We applied absolute flux scales to the complex gain solutions. Finally, we applied all the obtained calibration tables to the science targets.

### 3.2. Imaging

We performed multi-frequency synthesis (mfs) imaging (Rau & Cornwell 2011) using the CASA 6.4 `tclean` task. For the observations on each target at each frequency band, we produced one image using the aggregate bandwidth at that frequency band. We adopted natural weighting (Robust=2.0) to ensure the best continuum sensitivity.

In the X and C band observations, there are bright sources that are located outside of the  $\sim 4'$  and  $7'$  primary beam FWHM. Imaging with the default primary beam gain cutoff (`pblimit=0.2`) failed to recover them, which led to imaging

**Table 4.** Flux density measurements

Source	$F_{6.8\text{ GHz}}$	$\Delta F_{6.8\text{ GHz}}$	$F_{10.0\text{ GHz}}$	$\Delta F_{10.0\text{ GHz}}$	$F_{21.0\text{ GHz}}$	$\Delta F_{21.0\text{ GHz}}$	$F_{33.0\text{ GHz}}$	$\Delta F_{33.0\text{ GHz}}$	$F_{44.0\text{ GHz}}$	$\Delta F_{44.0\text{ GHz}}$
	(mJy)	(mJy)	(mJy)	(mJy)	(mJy)	(mJy)	(mJy)	(mJy)	(mJy)	(mJy)
AA Tau	< 0.037	–	< 0.101	–	< 0.17	–	0.31	0.06	0.49	0.11
AB Aur	0.171	0.035	0.115	0.035	0.38	0.05	0.69	0.10	0.82	0.07
BP Tau	–	–	< 0.074	–	–	–	0.28	0.04	0.52	0.11
CI Tau	< 0.035	–	< 0.109	–	< 0.16	–	0.53	0.08	0.91	0.18
CW Tau	–	–	0.095	0.031	–	–	0.71	0.09	1.00	0.24
CY Tau	< 0.164	–	0.149	0.050	< 0.30	–	0.88	0.12	1.68	0.06
DE Tau	–	–	< 0.032	–	–	–	0.41	0.04	0.71	0.16
DL Tau	< 0.082	–	< 0.119	–	< 0.34	–	0.93	0.05	2.54	0.44
DM Tau	< 0.038	–	< 0.098	–	0.14	0.02	0.51	0.06	0.69	0.05
DN Tau	< 0.045	–	< 0.102	–	0.31	0.07	0.55	0.10	1.17	0.07
DO Tau	< 0.129	–	< 0.106	–	< 0.46	–	1.29	0.15	1.73	0.27
DQ Tau	0.192	0.042	0.156	0.036	0.69	0.08	1.40 <sup>a</sup>	0.05 <sup>a</sup>	1.86	0.24
DR Tau	0.061	0.017	< 0.103	–	0.24	0.02	0.61	0.07	1.39	0.06
DS Tau	–	–	< 0.044	–	–	–	0.16	0.02	0.21	0.05
FT Tau	< 0.076	–	< 0.105	–	< 0.41	–	1.29	0.24	2.00	0.21
GM Aur	< 0.062	–	< 0.106	–	0.21	0.02	0.70	0.03	1.12	0.33
GO Tau	< 0.054	–	0.111	0.037	0.23	0.07	0.31	0.08	0.48	0.12
Haro 6-37	< 0.221	–	< 0.073	–	0.24	0.04	0.40	0.08	1.03	0.09
Haro 6-39	–	–	0.064	0.010	–	–	0.16	0.02	< 0.28	–
IP Tau	–	–	< 0.029	–	–	–	0.14	0.02	0.21	0.04
IQ Tau	< 0.066	–	< 0.098	–	0.20	0.05	0.38	0.05	0.76	0.17
LkCa 15	< 0.025	–	< 0.103	–	0.16	0.04	0.38	0.06	0.66	0.15
MHO 1/2	0.167	0.031	–	–	2.07	0.67	3.46	0.46	4.67	0.50
RY Tau	0.197	0.046	0.370	0.058	0.62	0.17	2.27	0.24	3.14	0.26
SU Aur	–	–	0.110	0.016	–	–	0.70	0.02	0.98	0.05
T Tau	7.162	0.053	7.187	0.086	29.77	0.39	14.63	0.37	15.80	0.59
UX Tau	0.183	0.024	< 0.077	–	0.56	0.16	0.79	0.11	1.32	0.06
UY Aur	0.110	0.030	0.150	0.018	0.54	0.10	1.03	0.05	2.41	0.26
UZ Tau	0.104	0.031	0.203	0.041	0.53	0.14	1.41	0.28	2.10	0.50
V710 Tau	0.490	0.021	< 0.068	–	0.28	0.04	0.57	0.08	0.61	0.12
V836 Tau	–	–	< 0.247	–	–	–	0.38	0.04	0.69	0.11
V892 Tau	0.381	0.050	0.683	0.068	1.92	0.31	3.75	0.28	4.38	0.31

<sup>a</sup>DQ Tau shows varying Ka band flux densities between the JVLA observations on 2010 08 21 and 2010 11 01. The recorded  $F_{33.0\text{ GHz}} = 1.40 \pm 0.04$  mJy on the table is taken on 2010 11 01, and on 2010 08 21 the  $F_{33.0\text{ GHz}} = 57.24 \pm 1.63$  mJy.

NOTE— The  $F$  and  $\Delta F$  represent the measured flux density and the 1- $\sigma$  error of flux density which includes the absolute flux uncertainties. The upper limit indicates the 3- $\sigma$  detection limit for the flux density. The hyphen symbol implies no observations on the source at that frequency.

artifacts. To amend this issue, we performed widefield imaging for the X and C band data using a image size that is  $4\times$  larger than the primary beam FWHM, by setting the keyword `gridded='widefield'` and `pblimit=-0.2`.

Some target sources were observed multiple times at certain frequency bands. To assess the data quality (e.g. residual phase error, rms noise level) of individual tracks of observations, we first imaged those tracks of observations separately and then compared the flux densities of the science target. For each target source, we omitted the tracks in which the target has  $<3\text{-}\sigma$  detection, and omitted the tracks that high residual phase errors led to inconsistent flux measurements with the other tracks. Moreover, we identified

the target sources which presented flux variability that is higher than 3 times the nominal 10% flux density uncertainty, and left out the flux measurements in the flaring period. The flaring period is determined by the epoch when the flux density is  $>2$  times larger than the average flux at other epochs. After verifying the consistency of flux densities, we jointly imaged the tracks at the same band to enhance the signal-to-noise ratio (SNR). The achieved synthesized beams and rms noise of the final images are summarized in Table 3.

### 3.3. Measuring Flux Densities

We derived flux densities at each JVLA band based on (1) 2D Gaussian fitting, or (2) directly reading pixel values in

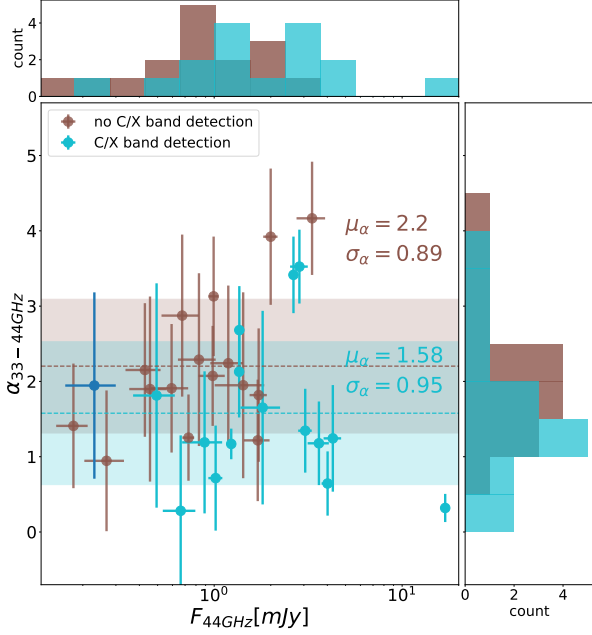


**Figure 5.** The Ka-Q band spectral index ( $\alpha_{33-44\text{ GHz}}$ ) versus the JVLA Q band (44 GHz) flux density ( $F_{44\text{ GHz}}$ ). Cyan points in the scatter plot show the sources that were detected either in the C band (5.8 GHz; Section 2.3) observations of the Disk@EVLA project or in our new X band (10 GHz; Section 2.2) observations (i.e., radio detected sources). Blue point shows one of the radio detected sources, Haro 6-39, for which we adopted the  $3\text{-}\sigma$  upper limit of  $F_{44\text{ GHz}}$ . The other sources are shown by brown points in the scatter plot (i.e., radio non-detected sources). Cyan/brown horizontal dashed lines and shaded areas in the scatter plot represent the means ( $\mu_\alpha$ ) and standard deviations ( $\sigma_\alpha$ ) of the  $\alpha_{33-44\text{ GHz}}$  of the radio detected/non-detected sources, respectively, which are also labeled in text. Histograms of  $\alpha_{33-44\text{ GHz}}$  and  $F_{44\text{ GHz}}$  for the radio detected and non-detected sources are shown in the right and top panels. The  $F_{44\text{ GHz}}$  values have been rescaled to a distance of 140 pc, which makes them different from the directly measured flux densities listed in Table 4.

the clean images. For images in which the target source was detected at  $>5\text{-}\sigma$ , we obtained the integrated flux density by performing 2D Gaussian fitting in a square region, using the CASA 6.4 `imfit` task. The square region is centered at the peak of the target source, and the side-length is  $\sim 5$  times the major axis of the synthesized beam. For images where the source was detected at  $3\text{-}\sigma$  significance, we reported the peak intensity as the flux density. For non-detections, we recorded the  $3\text{-}\sigma$  detection limits instead. We note that the hierarchical quadruple system, UZ Tau, was marginally spatially resolved into two components at Q band but was not resolved at lower frequencies. Following the approach of the previous SMA survey (Chung et al. 2024), we fit the UZ Tau system with one Gaussian regardless of the multiplicity. The binary system, MHO 1/2, was resolved at 44 GHz, marginally resolved at 33 and 21 GHz, but was

not resolved at lower frequencies. At  $\leq 33$  GHz, we fit the MHO 1/2 system with one Gaussian; at 44 GHz, we reported the summed flux of the two components. The flux densities measurements are summarized in Table 4. For a few sources that the Ka and Q band flux density measurements made out of the Disk@EVLA data have been reported by previous studies (DR Tau: Tazzari et al. 2016; CY Tau: Pérez et al. 2015; UZ Tau: Tripathi et al. 2018; AB Aur: Rodríguez et al. 2014), our flux density measurements made out of the same Disk@EVLA data achieved good consistency with those previous studies. This justifies the robustness of our data processing (Section 3).

## 4. RESULTS

### 4.1. Individual spectra

Figure 2–4 compare the flux density measurements obtained from the JVLA observations detailed in Sections 2.2 and 2.3, the recent SMA 200–400 GHz survey (Chung et al. 2024), and some flux density measurements reported over the past 20 years. Spectral indices were evaluated based on the flux density measurements from two adjacent bands. The uncertainties of the spectral indices were estimated using standard error propagation. In the upper left of each panel in Figure 2–4, we have labeled the inter-band spectral indices: the spectral indices between JVLA Ka and Q band ( $\alpha_{33-44\text{ GHz}}$ ), the spectral indices between JVLA K and Ka band ( $\alpha_{21-33\text{ GHz}}$ ), the spectral indices between JVLA Q band and SMA 200 GHz band ( $\alpha_{44-200\text{ GHz}}$ ), and the submillimeter spectral indices ( $\alpha_{200-400\text{ GHz}}$ ) quoted from Chung et al. (2024).

### 4.2. Spectra of variable sources

From the 32 disks sample, we found DQ Tau, T Tau, UZ Tau, AB Aur and UX Tau show strong radio flux variability (at any epoch the measured flux density is  $>2$  times larger or smaller than that at other epochs or the interpolated flux from the adjacent frequency bands). We also found some sources, DL Tau, DR Tau, CY Tau, LkCa 15, GO Tau and V710 Tau, show potential radio flux variability. The flux densities of DQ Tau at  $\gtrsim 200$  GHz are varying with time, which were resolved in the previous observations of Salter et al. (2010) and Chung et al. (2024). The 33 GHz flux density of DQ Tau also shows variability when comparing the two epochs of JVLA Ka band observations in August and November, 2010. Since the flux density of these two Ka band observations are different by two orders of magnitude, we did not image them jointly. Instead, they were imaged and plotted separately in (Figure 2). Another source, T Tau, also exhibits significant radio flux variability, which is evident when comparing different epochs (August 20 and 23, 2010) of JVLA observations at frequencies below 50 GHz (see Figure 4). We note that DQ Tau and T Tau are both multiple systems – DQ Tau is a spectroscopic binary, and T Tau is a triple system. UZ Tau and AB Aur also show radio flux variability at  $<10$  GHz as the C band flux densities measured in July, 2010 and the X band flux densities measured in September, 2022 are  $>3\text{-}\sigma$  different

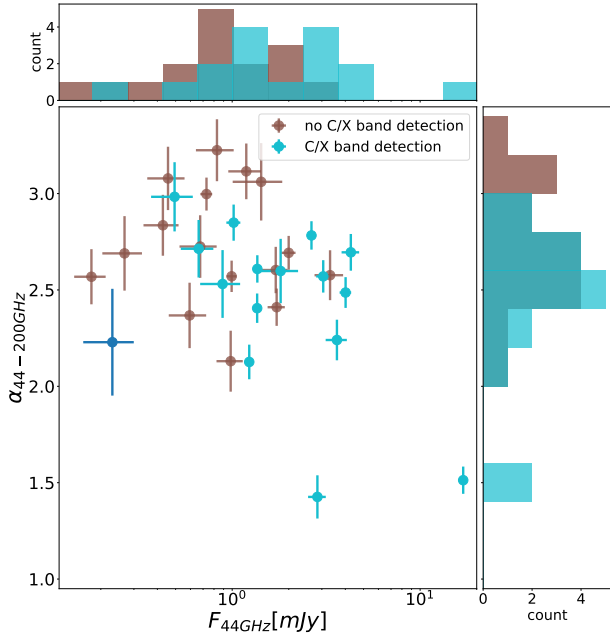


**Figure 6.** The Q band-200 GHz spectral index ( $\alpha_{44-200\text{GHz}}$ ) versus the JVLA Q band (44 GHz) flux density ( $F_{44\text{GHz}}$ ). Color codes and symbols are similar to those in Figure 5. Histograms of  $\alpha_{44-200\text{GHz}}$  and  $F_{44\text{GHz}}$  for the radio detected and non-detected sources are shown in the right and top panels, respectively. The  $F_{44\text{GHz}}$  values have been rescaled to a distance of 140 pc, which makes them different from the directly measured flux densities listed in Table 4.

from those reported by Rodmann et al. (2006), Rodríguez et al. (2014), Dzib et al. (2015) and Tripathi et al. (2018). In addition, DL Tau, DR Tau, CY Tau, LkCa 15, UX Tau, GO Tau and V710 Tau, were not detected either in the C band observations in the Disk@EVLA observations in 2010 or in our new X band observations in 2022, while they were detected in other observations at similar frequencies (e.g., Dzib et al. 2015; Zapata et al. 2017). These sources may also exhibit radio variability at  $<10$  GHz. The millimeter and radio variabilities of these sources are noteworthy. Previous JVLA monitoring observations (e.g., Liu et al. 2014; Dzib et al. 2015; Coutens et al. 2019) indicated that significant radio flares are not common during the Class II stage. Our present new results reinforce that to diagnose the emission of grown dust at centimeter band with spatially unresolved spectra, it is more robust if one can simultaneously constrain the flux densities of dust thermal emission and free-free or synchrotron emission.

#### 4.3. Spectra of sources not yet confirmed as millimeter/radio variables

Apart from the variable sources noted above, the  $>10$  GHz flux densities measured in different epochs of interferometric observations are in good agreement. Previous single-dish observations made with the Green Bank Telescope (Greaves & Mason 2022) showed systematically lower flux densities

in many, but not all cases (Figure 2–4), which could be attributed to data calibration issues.

The Disk@EVLA observations we analyzed detected C band emission in the following 11 sources: UY Aur, DR Tau, UX Tau, UZ Tau, RY Tau, MHO 1/2, DQ Tau, AB Aur, V892 Tau, T Tau, and V710 Tau. This indicates that the K, Ka, and Q band flux densities measured from the Disk@EVLA data may have been influenced by free-free or synchrotron emission, as these observations were conducted within a short time frame of each other (Table 2). The C band Disk@EVLA data we processed had high rms noise. Therefore, the K, Ka, and Q band flux densities measured from the Disk@EVLA data might still be influenced by free-free or synchrotron emission, even if the sources were not detected at C band. For instance, the 4 sources, DL Tau, CY Tau, LkCa 15 and GO Tau were not detected in the C band observations of the Disk@EVLA project, but were detected at similar frequencies in later observations reported by Dzib et al. (2015) and Zapata et al. (2017), and by our new X band observations. The K, Ka, and Q band flux densities of these four sources measured from the Disk@EVLA data might also be influenced by free-free or synchrotron emission; another possibility is that the free-free and/or synchrotron emission was not prominent during the Disk@EVLA K, Ka, and Q bands observations but becomes stronger during the later JVLA observations.

Among the 8 sources that we performed new JVLA X, Ka, and Q band observations, we detected X band emission from 3 of them: Haro 6-39, CW Tau, SU Aur (Section 2.2). As these X, Ka, and Q band observations were taken during a similar time period (Table 1), the Ka and Q band flux densities of these three sources were likely partly contributed by free-free or synchrotron emission. Furthermore, recent JVLA X and Ku band observations indicate significant free-free emission from DM Tau (Terada et al. 2023; Liu et al. 2024b). We also observed time variations of free-free or synchrotron emission in some of the sources, which can be seen when comparing our observations with those from previous studies (Figure 2–4). For sources that present strong free-free emission, the spectral index  $\alpha_{21-33\text{GHz}}$  may be smaller than  $\alpha_{33-44\text{GHz}}$ . On the other hand, in cases where  $\alpha_{21-33\text{GHz}}$  is higher than  $\alpha_{33-44\text{GHz}}$ , all of the three emission mechanisms, free-free, synchrotron, or dust emission may contribute significantly.

With our data in hand, it is not possible to quantitatively assess the fractional contribution of free-free emission at Ka and Q bands using a uniform approach. We are subject to this issue since our experimental design assumed that free-free emission is mostly optically thin at  $\gtrsim 6$  GHz frequencies, which had been a common approach. If it is indeed this case, we can extrapolate the flux densities of free-free emission from C or X band to higher frequencies based on an assumption of spectral indices  $\alpha \sim 0$  (Reynolds 1986). However, from none of the observed sources we found evidence that this assumption is true (Figure 2–4). Instead, from the sources that the free-free emission was relatively well constrained by the present observations (e.g. LkCa 15,

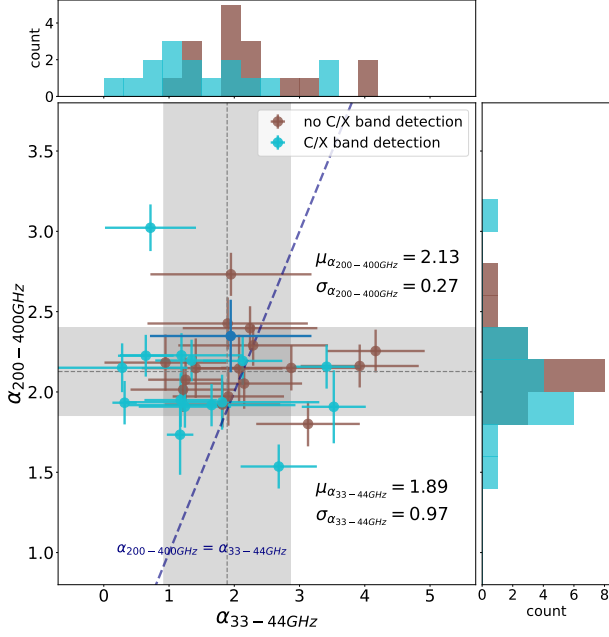


**Figure 7.** The Ka-Q band spectral index ( $\alpha_{33-44\text{GHz}}$ ) versus the submillimeter spectral index ( $\alpha_{200-400\text{GHz}}$ ) quoted from Chung et al. (2024). Color codes and symbols are similar to those in Figure 5. Gray vertical and horizontal dashed lines (and shaded areas) in the scatter plot represent the means ( $\mu_\alpha$ ) (and standard deviations ( $\sigma_\alpha$ )) of the  $\alpha_{33-44\text{GHz}}$  and  $\alpha_{200-400\text{GHz}}$  of all the sources, respectively, which are also labeled in text. The dark blue dashed line shows where the two spectral indices are equal. Histograms of  $\alpha_{200-400\text{GHz}}$  and  $\alpha_{33-44\text{GHz}}$  for the radio detected and non-detected sources are shown in the right and top panels.

RY Tau, DQ Tau, AB Aur, V892 Tau), we found that the spectral indices are considerably higher than 0, indicating that free-free emission may be partly optically thick. In these cases, extrapolating flux densities of free-free emission from C and X bands to higher frequencies based on an optically thin assumption will lead to significant underestimates. The observations we utilized only made measurements at one of the C (6 GHz) and X (10 GHz) bands during a similar time period, not both. Therefore, we did not obtain good constraints on the optical depth of free-free emission. The extrapolation to higher frequency then becomes largely arbitrary. Nevertheless, it is still possible to qualitatively discuss the fractional contribution of free-free emission at 30–50 GHz based on the distribution of the spectral indices  $\alpha_{33-44\text{GHz}}$  (more below).

#### 4.4. Spectral variations and transition regions across 50–200 GHz

We observed a wide range of spectral indices  $\alpha_{33-44\text{GHz}}$ , varying from 0.3 to 4.2 (see Figure 5), with most values clustered around  $\sim 2.0$ , but showing some prominent outliers. This indicates a broader scatter compared to the more narrowly concentrated distribution of the 200–400 GHz spectral index,  $\alpha_{200-400\text{GHz}} \sim 2.0$ , reported in the SMA survey

(Chung et al. 2024). In most cases, the flux densities at frequencies below 50 GHz are lower than the extrapolation from 200–400 GHz based on a constant spectral index assumption (see Figure 2–4). This suggests that there are transitional regions in the spectra between 50–200 GHz frequencies where the flux densities rapidly increase with frequency. In these transition regions, the spectral indices may be around 3–4, although they are not spectrally resolved in all observed cases (more below). The observed  $\alpha_{44-200\text{GHz}}$  of most sources lies between 2.0 and 3.5 (Figure 6), which is likely a consequence of averaging the high spectral indices in the transition regions and the lower spectral indices at frequencies higher and lower than those of the transition regions.

Incorporating the previous flux density measurements taken between 50 GHz and 200 GHz frequencies helps in gaining a better understanding of the spectral profiles in the transition regions (50–200 GHz). In some cases, such as BP Tau (Figure 2), we observed that the spectral profile, resolved at 200–400 GHz smoothly transitions to a sharp turning point at  $\sim 100$  GHz. In this case, there is another turning point at  $\gtrsim 50$  GHz where the spectral index rapidly increases with frequency. The frequency ranges of the transition regions (or the frequencies of the turning points) change from source to source (Appendix A). For example (Figure 3), in the spectra of Haro 6-37 and UY Aur, we resolved relatively steep transitions at  $\sim 35$ –50 GHz; the transition regions are close to 90–110 GHz in the cases of BP Tau and CI Tau; the transition regions are close to 150 GHz in the cases of CY Tau and DE Tau, etc. In the cases of IQ Tau and AA Tau, the frequencies of the transition regions are loosely constrained to be in the range of 50–200 GHz, due to the lack of observations at 90–150 GHz. For all of the selected sources, the frequencies of the transition regions can be better determined by performing Northern Extended Millimetre Array (NOEMA) Band 1 (70.384–119.872 GHz) and Band 2 (127.000–182.872 GHz) observations and/or ALMA Band 3 (84–116 GHz), 4 (125–163 GHz), and 5 (163–211 GHz) observations.

#### 4.5. Statistical results

Figure 5 and 6 show the  $\alpha_{33-44\text{GHz}}$  and  $\alpha_{44-200\text{GHz}}$  of all 32 sources in the selected sample, which are plotted against the Q band flux density. For Haro 6-39, which was not detected in Q band, we adopted the  $3\text{-}\sigma$  upper limit as the Q band flux density in statistical analysis. To assess whether or not free-free and/or synchrotron emission was prominent during the Ka and Q band observations (Sections 2.2, 2.3), we distinguished the 16 sources detected in the C band observations of the Disk@EVLA project or in our X band observations as "radio detected sources," while the remaining samples were referred to as "radio non-detected sources".

We observed that a significant portion of the radio non-detected sources have  $\alpha_{33-44\text{GHz}}$  values consistent with 2.0 (Figure 5). On the other hand, the radio detected sources show systematically lower  $\alpha_{33-44\text{GHz}}$  values. Moreover, sources with low  $\alpha_{33-44\text{GHz}}$  values tend to be bright Q band

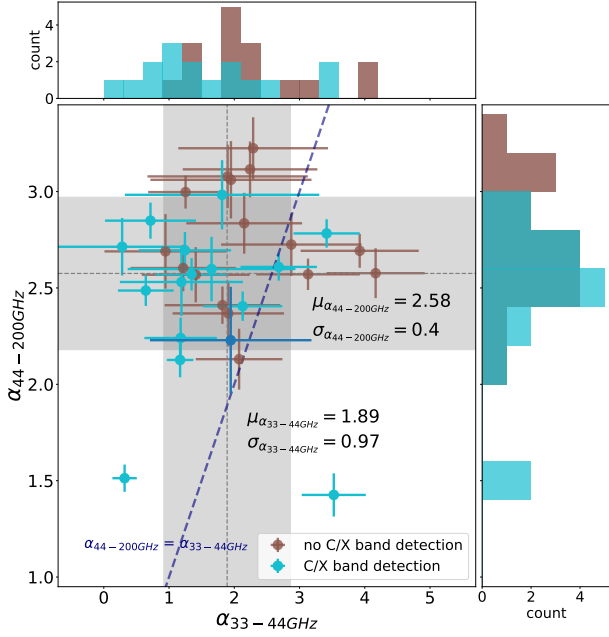


**Figure 8.** The Ka-Q band spectral index ( $\alpha_{33-44\text{GHz}}$ ) versus the Q band-200 GHz spectral index ( $\alpha_{44-200\text{GHz}}$ ). Color codes and symbols are similar to those in Figure 5. Gray vertical and horizontal dashed lines (and shaded areas) in the scatter plot represent the means ( $\mu_\alpha$ ) (and standard deviations ( $\sigma_\alpha$ )) of the  $\alpha_{33-44\text{GHz}}$  and  $\alpha_{44-200\text{GHz}}$  of all the sources, respectively, which are also labeled in text. The dark blue dashed line shows where the two spectral indices are equal. Histograms of  $\alpha_{44-200\text{GHz}}$  and  $\alpha_{33-44\text{GHz}}$  for the radio detected and non-detected sources are shown in the right and top panels.

emitters. As a result, the radio detected sources tend to occupy the lower right part of Figure 5, while the radio non-detected sources tend to occupy the upper left part of that figure. However, we note that both sub-samples exhibit a similarly large scatter.

The  $\alpha_{44-200\text{GHz}}$  values are distributed in a narrower range of 2.0–3.5 than that of  $\alpha_{33-44\text{GHz}}$  (Figure 6). Most radio detected and non-detected sources have comparable  $\alpha_{44-200\text{GHz}}$ . Exceptions are the variable sources, T Tau, which has  $\alpha_{33-44\text{GHz}} = 1.51 \pm 0.07$  (Figure 4); and UY Aur, which has  $\alpha_{33-44\text{GHz}} = 1.43 \pm 0.11$  (Figure 2).

To examine the change in spectral index from submillimeter to millimeter wavelengths, we compare  $\alpha_{33-44\text{GHz}}$  with  $\alpha_{200-400\text{GHz}}$ ,  $\alpha_{44-200\text{GHz}}$  with  $\alpha_{33-44\text{GHz}}$ , and  $\alpha_{44-200\text{GHz}}$  with  $\alpha_{200-400\text{GHz}}$  in Figure 7, Figure 8, and Figure 9, respectively. In Figure 7, the  $\alpha_{200-400\text{GHz}}$  are concentrated to a narrow range of  $2.1 \pm 0.3$ , which is consistent with the measurement for a larger sample reported by Chung et al. (2024). We do not observe any significant differences in the  $\alpha_{200-400\text{GHz}}$  values between the radio-detected and non-detected sources, although this may be partly due to our limited sample size. In general, at frequencies  $>200\text{GHz}$ , free-free and synchrotron emission are likely

negligible compared to dust emission, although there are exceptions (e.g., DQ Tau, Salter et al. 2010; Chung et al. 2024). In Figure 9, most of the sources, especially the radio non-detected sources, show higher  $\alpha_{44-200\text{GHz}}$  than  $\alpha_{200-400\text{GHz}}$ . In most of the sources,  $\alpha_{44-200\text{GHz}}$  is also higher than  $\alpha_{33-44\text{GHz}}$  (Figure 8). As discussed in Section 4.4, this indicates that in a spectrum, there is a transition region between 50–200 GHz where the spectral index is high (approximately 3–4). In over 50% of our sample, the value of  $\alpha_{33-44\text{GHz}}$  is lower than  $\alpha_{200-400\text{GHz}}$ , which is contrary to the trend expected from a single emission component that has a dust origin (cf. Hildebrand 1983; Liu 2019, and references therein; for more discussion see the following section).

## 5. DISCUSSION

### 5.1. Characterizing the 20–400 GHz broadband spectra of the Class II disks

In our present study, we expect that dust emission dominates at  $>200\text{GHz}$  frequencies. At  $<100\text{GHz}$ , it appears that both dust emission and free-free/synchrotron emission may be prominent, which are not clearly distinguished from the present observations. In most of our observed cases, this hinders fitting with physical functions. For example, the source CI Tau (in Figure 2) has 2 constraints and 3 upper limits at  $<50\text{GHz}$  frequency, and some constraints at  $>90\text{GHz}$ . At frequencies below 50 GHz, it is possible to fit the data using a dust emission spectrum or a combination of dust and free-free emission, while the resulting parameters are too degenerate to yield any meaningful physical interpretation. Although the fitting functions themselves are physically motivated, the parameters derived from these fits are not. The spectral index is the only concrete information in this frequency range.

In addition, when extrapolating the fitting from frequencies below 50 GHz to above 90 GHz, there is an arbitrary choice of whether (i) the dominant emitter of  $<50\text{GHz}$  emission should be obscured by the dust emission source that dominates the  $>200\text{GHz}$  spectrum, or (ii) we should simply coadd the emission from the emission sources, assuming no mutual obscuration. These arbitrary choices make it difficult to extract further information beyond the spectral index and the transition frequency. The sources, V836 Tau (Figure 2), GM Aur, Haro 6-39, AA Tau, DE Tau, FT Tau (Figure 3), and many others, are subject to the same problem as CI Tau. BP Tau may allow fitting a physical function at  $>90\text{GHz}$ , while the lower frequency can only be characterized by a power-law with no physical meaning.

For most sources, the observed spectra at  $\gtrsim 20\text{GHz}$  can be characterized by two power laws connected by a sigmoid function (Figure 2–4; Table 5), which are detailed in Appendix A. The fittings in Appendix A characterized the spectral indices at high and low frequencies, the frequency of the transition regions, and the steepness of the transition. The spectral profiles at  $<20\text{GHz}$  are more complicated, which may be due to the contribution of multiple emission mechanisms (e.g., free-free, synchrotron, and dust) and their potential variability. The transition region is necessary

because the intersection of the two power laws does not naturally meet in the middle.

To characterize the transition region, we chose to use a sigmoid function in this paper to systematically derive the transitional frequency without explicitly deriving the spectral index in the transition region. The spectral index in this range likely lacks physical meaning due to the mixed contributions of different emission mechanisms. While alternative approaches, such as piecewise power-law fits, could also characterize this region, the sigmoid function provides a practical and systematic framework for estimating the transition frequency. We note that piecewise power-laws fit (as well as other similar approaches) are not necessarily more physical than connecting two power-laws with a sigmoid function, in the sense that the slopes of the piecewise power-laws are step functions. On the contrary, the functional form of the sigmoid function allows a relatively smooth transition (e.g., the cases of DL Tau and LkCa 15 in Figure 2, etc).

It is important to note that the sigmoid function is not intended to imply a physically meaningful model for the transition but rather provides a practical and systematic framework for estimating the transition frequency. We also note that due to the lack of data points in the transition region, the slope of the transition cannot be reliably constrained, as shown in Figures 2–4 and Table 5. Our conclusions, particularly the differences in emission components between high and low frequencies, remain unaffected by the choice of transition model.

When the data are more complete, we can do a fairly sophisticated fitting of dust thermal emission (e.g., DM Tau, Liu et al. 2024b). In general, the data presented in this study provide useful constraints on certain physical parameters, such as the spectral index at 20–50 GHz, at 200–400 GHz, and the transition frequency. However, deriving physical insights in a uniform and systematic way across all sources remains challenging. We aim to address these complexities in follow-up case studies of individual sources as additional data become available.

### 5.2. Interpretation of emission components in Class II disk spectra and their implications

In general, the 4–400 GHz broadband spectra of the Class II protoplanetary disks in the Taurus-Auriga region require at least two distinct emission components for interpretation. The first is the dust emission in the bulk of the disk that dominates the emission at >200 GHz frequencies. Other components (e.g., high-density dust crescents or clumps, free-free emission, synchrotron emission, and emission from spinning nanometer-sized dust, c.f. Hildebrand 1983; Liu 2019; Reynolds 1986; Anglada et al. 1998; Güdel 2002; Hoang et al. 2018) dominate at lower frequencies.

In the case of radio non-detected sources, flux densities in the 30–50 GHz range with  $\alpha_{33-44 \text{ GHz}} \sim 2$  indicate either dust emission, optically thick free-free emission, or a combination of both. For the radio detected sources, the consistently lower  $\alpha_{33-44 \text{ GHz}}$  values (Figure 5) suggest that

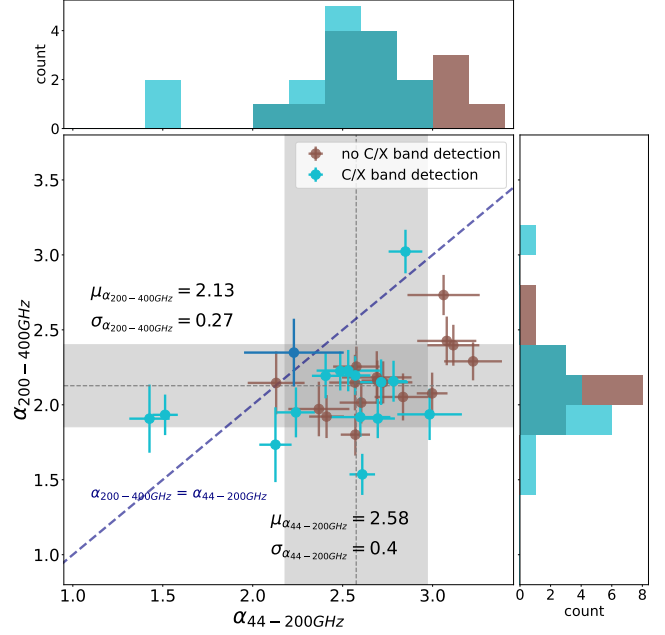


**Figure 9.** The Q band-200 GHz spectral index ( $\alpha_{44-200\text{GHz}}$ ) versus the submillimeter spectral index ( $\alpha_{200-400\text{GHz}}$ ) quoted from Chung et al. (2024). Color codes and symbols are similar to those in Figure 5. Gray vertical and horizontal dashed lines (and shaded areas) in the scatter plot represent the means ( $\mu_\alpha$ ) (and standard deviations ( $\sigma_\alpha$ )) of the  $\alpha_{44-200\text{GHz}}$  and  $\alpha_{200-400\text{GHz}}$  of all the sources, respectively, which are also labeled in text. The dark blue dashed line shows where the two spectral indices are equal. Histograms of  $\alpha_{200-400\text{GHz}}$  and  $\alpha_{44-200\text{GHz}}$  for the radio detected and non-detected sources are shown in the right and top panels.

the 30–50 GHz flux densities are partly due to optically thin free-free emission (Reynolds 1986; Anglada et al. 1998) or synchrotron emission (Güdel 2002). Dust thermal emission could be significant in this frequency range.

For dust thermal emission to have  $\alpha_{33-44 \text{ GHz}} \sim 2$ , the dust emission source needs to have either very high optical depth or very large  $a_{\text{max}}$  (Hildebrand 1983). Besides, high optical depths could be achieved by concentrating a lot of dust mass, another possibility to locally enhance the dust optical depth may be dust grain growth that yields millimeter-centimeter grain sizes. In this case, the dust absorption opacities can be maximized at 33–44 GHz. Otherwise, including some specific form of carbonaceous dust (e.g. graphite or certain types of amorphous dust) in the dust composition (i.e. segregation of dust composition) may also significantly enhance the dust absorption opacity, although it is not yet clear how much of these materials can be included (see the discussion in Draine 2006).

Further complexity arises across the snow line, a transition boundary where dust composition and spectral index can change rapidly, as noted by Testi et al. (2014). Such

**Table 5.** Observed spectral indices and best fit parameters in spectrum fitting

Source	$\alpha_{33-44\text{ GHz}}$	$\alpha_{200-400\text{ GHz}}$	$\alpha_{44-200\text{ GHz}}$	$\alpha_{\text{mm}}$	$\alpha_{\text{submm}}$	$\omega$	$b/\omega$ (GHz)
AA Tau	$1.9 \pm 1.23$	$2.43 \pm 0.16$	$3.08 \pm 0.16$	$2.38^{+1.1}_{-1.09}$	$2.43^{+0.17}_{-0.17}$	$0.23^{+0.049}_{-0.153}$	$118.52^{+45.22}_{-43.51}$
AB Aur	$0.72 \pm 0.7$	$3.02 \pm 0.15$	$2.85 \pm 0.09$	$1.11^{+0.62}_{-0.42}$	$3.02^{+0.13}_{-0.14}$	$0.349^{+0.127}_{-0.086}$	$67.91^{+17.17}_{-15.47}$
BP Tau	$2.15 \pm 0.89$	$2.05 \pm 0.16$	$2.84 \pm 0.16$	$2.37^{+0.82}_{-0.82}$	$2.04^{+0.16}_{-0.15}$	$0.274^{+0.027}_{-0.07}$	$90.59^{+2.08}_{-1.26}$
CI Tau	$2.24 \pm 1.03$	$2.4 \pm 0.14$	$3.12 \pm 0.14$	$2.39^{+0.94}_{-0.97}$	$2.4^{+0.14}_{-0.13}$	$0.066^{+0.131}_{-0.054}$	$111.29^{+2.83}_{-2.13}$
CW Tau	$1.19 \pm 0.94$	$2.23 \pm 0.14$	$2.53 \pm 0.18$	$1.47^{+0.78}_{-0.63}$	$2.2^{+0.11}_{-0.12}$	$0.169^{+0.047}_{-0.096}$	$100.83^{+13.88}_{-9.69}$
CY Tau	$2.68 \pm 0.58$	$1.54 \pm 0.14$	$2.61 \pm 0.07$	$2.71^{+0.59}_{-0.56}$	$1.54^{+0.13}_{-0.13}$	$0.289^{+0.097}_{-0.118}$	$165.15^{+24.75}_{-27.53}$
DE Tau	$1.91 \pm 0.85$	$1.97 \pm 0.18$	$2.37 \pm 0.17$	$2.05^{+0.78}_{-0.8}$	$1.98^{+0.18}_{-0.17}$	$0.227^{+0.046}_{-0.153}$	$150.95^{+31.24}_{-32.64}$
DL Tau	$4.17 \pm 0.75$	$2.25 \pm 0.13$	$2.58 \pm 0.13$	$1.23^{+0.1}_{-0.09}$	$2.19^{+0.11}_{-0.11}$	$0.059^{+0.199}_{-0.009}$	$81.44^{+1.99}_{-1.86}$
DM Tau	$1.25 \pm 0.57$	$2.08 \pm 0.14$	$3.0 \pm 0.09$	$1.37^{+0.58}_{-0.48}$	$2.09^{+0.13}_{-0.14}$	$0.118^{+0.107}_{-0.063}$	$105.4^{+3.42}_{-3.84}$
DN Tau	$3.13 \pm 0.79$	$1.8 \pm 0.14$	$2.57 \pm 0.08$	$1.67^{+0.76}_{-0.64}$	$1.8^{+0.13}_{-0.13}$	$0.072^{+0.146}_{-0.073}$	$75.6^{+36.81}_{-23.51}$
DO Tau	$1.22 \pm 0.81$	$2.01 \pm 0.14$	$2.6 \pm 0.12$	$1.44^{+0.66}_{-0.59}$	$2.01^{+0.13}_{-0.13}$	$0.136^{+0.094}_{-0.068}$	$76.97^{+4.22}_{-5.06}$
DQ Tau	$1.18 \pm 0.56$	$1.95 \pm 0.17$	$2.24 \pm 0.11$	$1.43^{+0.57}_{-0.54}$	$1.95^{+0.16}_{-0.17}$	$0.12^{+0.112}_{-0.081}$	$80.18^{+6.15}_{-11.25}$
DR Tau	$3.42 \pm 0.51$	$2.16 \pm 0.14$	$2.78 \pm 0.07$	$2.17^{+0.29}_{-0.33}$	$2.17^{+0.14}_{-0.13}$	$0.03^{+0.008}_{-0.007}$	$110.67^{+4.73}_{-4.1}$
DS Tau	$0.95 \pm 0.93$	$2.18 \pm 0.17$	$2.69 \pm 0.19$	$1.35^{+0.74}_{-0.55}$	$1.91^{+0.12}_{-0.13}$	$0.06^{+0.042}_{-0.028}$	$100.66^{+0.91}_{-1.06}$
FT Tau	$1.82 \pm 0.89$	$1.92 \pm 0.14$	$2.41 \pm 0.1$	$1.96^{+0.87}_{-0.76}$	$1.93^{+0.14}_{-0.13}$	$0.056^{+0.132}_{-0.053}$	$112.45^{+6.75}_{-3.59}$
GM Aur	$1.95 \pm 1.23$	$2.73 \pm 0.13$	$3.06 \pm 0.2$	$2.56^{+1.08}_{-1.13}$	$2.76^{+0.11}_{-0.12}$	$1.677^{+0.091}_{-0.611}$	$82.23^{+20.69}_{-24.79}$
GO Tau	$1.81 \pm 1.49$	$1.94 \pm 0.17$	$2.98 \pm 0.18$	$2.37^{+1.31}_{-1.09}$	$2.48^{+0.12}_{-0.14}$	$0.282^{+0.064}_{-0.084}$	$78.23^{+7.06}_{-20.13}$
Haro 6-37	$3.92 \pm 0.91$	$2.16 \pm 0.13$	$2.69 \pm 0.09$	$1.33^{+0.53}_{-0.45}$	$2.17^{+0.13}_{-0.14}$	$0.168^{+0.064}_{-0.138}$	$49.09^{+17.59}_{-4.53}$
Haro 6-39	$1.95 \pm 1.24$	$2.35 \pm 0.23$	$2.23 \pm 0.28$	$0.82^{+0.18}_{-0.18}$	$2.35^{+0.21}_{-0.22}$	$0.195^{+0.016}_{-0.155}$	$111.6^{+53.34}_{-51.25}$
IP Tau	$1.41 \pm 0.83$	$2.15 \pm 0.19$	$2.57 \pm 0.14$	$1.6^{+0.8}_{-0.67}$	$2.15^{+0.17}_{-0.18}$	$0.211^{+0.036}_{-0.161}$	$117.97^{+45.87}_{-45.46}$
IQ Tau	$2.87 \pm 1.08$	$2.15 \pm 0.14$	$2.73 \pm 0.16$	$1.93^{+1.12}_{-0.75}$	$2.15^{+0.13}_{-0.13}$	$0.23^{+0.051}_{-0.145}$	$118.54^{+45.24}_{-46.13}$
LkCa 15	$2.29 \pm 1.15$	$2.29 \pm 0.13$	$3.22 \pm 0.16$	$2.53^{+1.05}_{-1.04}$	$2.05^{+0.09}_{-0.09}$	$0.049^{+0.025}_{-0.017}$	$121.78^{+3.15}_{-2.87}$
MHO 1	$1.24 \pm 0.71$	$1.91 \pm 0.13$	$2.41 \pm 0.1$	$1.42^{+0.66}_{-0.55}$	$1.9^{+0.13}_{-0.12}$	$0.342^{+0.133}_{-0.089}$	$78.55^{+13.87}_{-17.45}$
RY Tau	$1.35 \pm 0.56$	$2.2 \pm 0.13$	$2.57 \pm 0.08$	$1.4^{+0.54}_{-0.49}$	$1.94^{+0.1}_{-0.1}$	$0.077^{+0.128}_{-0.055}$	$112.58^{+4.49}_{-2.06}$
SU Aur	$1.17 \pm 0.2$	$1.73 \pm 0.25$	$2.13 \pm 0.09$	$1.18^{+0.21}_{-0.22}$	$1.72^{+0.22}_{-0.23}$	$0.069^{+0.135}_{-0.062}$	$95.92^{+15.35}_{-8.14}$
T Tau	$0.32 \pm 0.19$	$1.93 \pm 0.14$	$1.51 \pm 0.07$	$0.62^{+0.12}_{-0.08}$	$1.93^{+0.14}_{-0.13}$	$0.112^{+0.11}_{-0.057}$	$96.76^{+8.63}_{-8.45}$
UX Tau	$2.13 \pm 0.61$	$2.19 \pm 0.15$	$2.41 \pm 0.08$	$2.15^{+0.69}_{-0.58}$	$2.19^{+0.16}_{-0.14}$	$0.076^{+0.157}_{-0.078}$	$88.94^{+9.09}_{-16.79}$
UY Aur	$3.52 \pm 0.49$	$1.91 \pm 0.23$	$1.43 \pm 0.11$	$1.46^{+0.47}_{-0.42}$	$1.48^{+0.07}_{-0.06}$	$0.782^{+0.13}_{-0.122}$	$38.52^{+1.33}_{-1.27}$
UZ Tau	$1.65 \pm 1.29$	$1.92 \pm 0.13$	$2.6 \pm 0.17$	$2.08^{+1.13}_{-0.94}$	$2.05^{+0.09}_{-0.09}$	$0.026^{+0.016}_{-0.01}$	$120.19^{+5.14}_{-4.59}$
V710 Tau	$0.28 \pm 1.0$	$2.15 \pm 0.15$	$2.71 \pm 0.15$	$1.11^{+0.72}_{-0.43}$	$2.15^{+0.15}_{-0.15}$	$0.24^{+0.057}_{-0.144}$	$121.24^{+44.14}_{-43.42}$
V836 Tau	$2.07 \pm 0.66$	$2.15 \pm 0.21$	$2.13 \pm 0.16$	$2.14^{+0.04}_{-0.04}$	$1.83^{+0.12}_{-0.11}$	$0.375^{+0.147}_{-0.072}$	$72.64^{+15.6}_{-15.46}$
V892 Tau	$0.64 \pm 0.43$	$2.23 \pm 0.13$	$2.49 \pm 0.08$	$0.84^{+0.34}_{-0.24}$	$2.22^{+0.13}_{-0.13}$	$0.399^{+0.15}_{-0.062}$	$70.75^{+15.85}_{-15.04}$

NOTE— $\alpha_{33-44\text{ GHz}}$ : spectral index between JVLA Ka band and Q band.  $\alpha_{200-400\text{ GHz}}$ : submillimeter spectral index quoted from Chung et al. (2024).  $\alpha_{44-200\text{ GHz}}$ : spectral index between JVLA Q band and SMA 200 GHz band.  $\alpha_{\text{mm}}$ : spectral index of the submillimeter power law,  $P_{\text{submm}}(\nu)$ .  $\alpha_{\text{submm}}$ : spectral index of the millimeter power law,  $P_{\text{mm}}(\nu)$ .  $\omega$ : steepness of transition in the sigmoid function.  $\sigma_{\omega,b}(\nu)$ ,  $b/\omega$ : mean frequency of the transition region in  $\sigma_{\omega,b}(\nu)$ .

transitions might be relevant for understanding changes in spectral index, which could exhibit distinct features tied to compositional changes across this line (e.g. Liu et al. 2021; Houge et al. 2024).

Our current understanding of the 4–400 GHz spectra (Section 4.4) and the statistical results (Section 4.5) suggests that the dust processing scenario described in Section 1 may be applicable in a good fraction of Class II protoplanetary disks. In the bulk of the disk, the emission is optically thick at 200–400 GHz, resulting in  $\alpha_{200-400\text{ GHz}} \sim 2.0$ . In certain disks that the observed spectra have allowed for sophisticated SED fittings (e.g., HD 163296, DM Tau; Guidi et al. 2022; Liu et al. 2024b), or in the disks where linearly polarized (sub)millimeter dust polarization have been detected (e.g.,

HL Tau, HD 163296, IM Lup, HD 142527, etc; Kataoka et al. 2016a; Stephens et al. 2023; Dent et al. 2019; Hull et al. 2018; Kataoka et al. 2016b), the 200–400 GHz emission in the bulk of these disks may be dominated by optically thick thermal emission of small dust grains (e.g.,  $a_{\text{max}} \sim 50\text{--}150 \mu\text{m}$ ). In the remaining disks, the 200–400 GHz emission in the bulk of the disks is consistent with being dominated by the optically thick thermal emission of small dust grains (e.g.,  $a_{\text{max}} \lesssim 0.1 \text{ mm}$ ), although the optically thick thermal emission of grown dust grains (e.g.,  $a_{\text{max}} \gtrsim 3 \text{ mm}$ ) is also consistent with the observations (c.g. Chung et al. 2024). In addition, in many disks, there are embedded substructures (regions of grown dust) with high  $\Sigma_{\text{dust}}$  and/or high  $a_{\text{max}}$  values. These dust substructures have small linear and

angular dimensions, and therefore contribute only a small fraction of the 200–400 GHz flux densities. As the bulk of the disk becomes optically thin at around 50–200 GHz, its flux density drops rapidly at low frequencies. Consequently, at  $\lesssim 50$  GHz, the flux densities of dust substructures become more prominent compared to the emission in the bulk of the disks. Such dust substructures may be distinguished from the free-free or synchrotron emission sources in high angular resolution imaging observations. The dust substructures may be important sites for forming planetesimals and rocky planets.

## 6. CONCLUSION

We have performed the JVLA X (8–12 GHz), Ka (29–37 GHz), and Q (40–48 GHz) observations towards 8 selected Class II protoplanetary disks in the Taurus-Auriga region. Comparing with the C (4.8–6.8 GHz), K (20.0–22.0 GHz), Ka (31.7–33.6 GHz), and Q (41.0–43.0 GHz) band observations taken from the Disk@EVLA project (PI: C. Chandler) in the C and D array configurations, the previous SMA 200–400 GHz survey (Chung et al. 2024), and various flux density measurement published over the last 20 years, we have compiled the 4–400 GHz spectra for 32 Class II protoplanetary disks in the Taurus-Auriga region. At submillimeter band, this sample represents the top 33 percentile of the brightest Class II disks observed in this region. We found that in general, the spectra at  $>20$  GHz frequency can be described with a piecewise function: a power law with spectral index  $\sim 2$  in the  $>200$  GHz region, a power law with spectral index in the range of 0.3–4.2 in the 20–50 GHz region, and a transition region in between these two power laws which can be characterized by a sigmoid function. This implies that the flux densities at  $>200$  GHz and  $<50$  GHz are dominated by distinct emission components. At  $>200$  GHz, the emission is likely dominated by the optically thick dust thermal emission in the bulk of the disks. In some sources that were not detected in the C and/or X band observations, the embedded, high-density (grown, e.g.,  $a_{max} \gtrsim 1$  mm) dust substructures may contribute to a significant fraction of the flux densities at 30–50 GHz, and thus there 30–50 GHz spectral indices are mostly consistent with 2.0. Among the selected samples, examples with previously spatially resolved high-density grown dust substructures include DM Tau (Liu et al. 2024b) and LkCa 15 (Isella et al. 2014). However, at 30–50 GHz, free-free and/or synchrotron emission may be significant. In

fact, the 30–50 GHz spectral indices of the bright Q band emitters in our sample tend to be systematically lower than 2.0, meaning that free-free emission and/or synchrotron are what made some sources bright at Q band. Based on these results, we hypothesize that the embedded, high-density grown dust substructures are often found in resolved Class II protoplanetary disks. Investigating these dust substructures may be a key to understanding the formation of kilometer-sized planetesimals and rocky planets. To robustly investigate the properties of the embedded dust structures, one need to carry out high angular resolution observations at  $\lesssim 50$  GHz band to separate them from the free-free and/or synchrotron emissions. Otherwise, in the analyses of the spatially unresolved spectra, one need to simultaneously constrain the spectral profiles of the dust emission, free-free emission, and synchrotron emission. Based on the present observations, we caution that, in general, free-free emission is not necessarily optically thin at  $>10$  GHz frequencies. To correctly assess the dust properties in the (grown) dust substructures, it is important to constrain the optical depths of free-free emission with the radio spectra that are well sampled in the frequency domain.

We thank the anonymous referee for useful suggestions. We thank Dr. Sean Andrews for useful discussion. The National Radio Astronomy Observatory is a facility of the National Science Foundation operated under cooperative agreement by Associated Universities, Inc. The Submillimeter Array is a joint project between the Smithsonian Astrophysical Observatory and the Academia Sinica Institute of Astronomy and Astrophysics and is funded by the Smithsonian Institution and the Academia Sinica. We recognize that Maunakea is a culturally important site for the indigenous Hawaiian people; we are privileged to study the cosmos from its summit. C.Y.C. and H.B.L. are supported by the National Science and Technology Council (NSTC) of Taiwan (Grant Nos. 111-2112-M-110-022-MY3, 113-2112-M-110-022-MY3).

*Facilities:* JVLA, ALMA, SMA

*Software:* astropy (Astropy Collaboration et al. 2022), Numpy (van der Walt et al. 2011), CASA (CASA Team et al. 2022), emcee (Foreman-Mackey et al. 2013),

## REFERENCES

- Acke, B., van den Ancker, M. E., Dullemond, C. P., van Boekel, R., & Waters, L. B. F. M. 2004, *A&A*, 422, 621, doi: [10.1051/0004-6361:20040197](https://doi.org/10.1051/0004-6361:20040197)
- Akeson, R. L., Jensen, E. L. N., Carpenter, J., et al. 2019, *ApJ*, 872, 158, doi: [10.3847/1538-4357/aaff6a](https://doi.org/10.3847/1538-4357/aaff6a)
- Andrews, S. M., Huang, J., Pérez, L. M., et al. 2018, *ApJL*, 869, L41, doi: [10.3847/2041-8213/aaf741](https://doi.org/10.3847/2041-8213/aaf741)
- Anglada, G., Villuendas, E., Estalella, R., et al. 1998, *AJ*, 116, 2953, doi: [10.1086/300637](https://doi.org/10.1086/300637)
- Astropy Collaboration, Price-Whelan, A. M., Lim, P. L., et al. 2022, *ApJ*, 935, 167, doi: [10.3847/1538-4357/ac7c74](https://doi.org/10.3847/1538-4357/ac7c74)
- Birnstiel, T. 2023, arXiv e-prints, arXiv:2312.13287, doi: [10.48550/arXiv.2312.13287](https://doi.org/10.48550/arXiv.2312.13287)

- Birnstiel, T., Dullemond, C. P., Zhu, Z., et al. 2018, *ApJL*, 869, L45, doi: [10.3847/2041-8213/aaf743](https://doi.org/10.3847/2041-8213/aaf743)
- Carrasco-González, C., Sierra, A., Flock, M., et al. 2019, *ApJ*, 883, 71, doi: [10.3847/1538-4357/ab3d33](https://doi.org/10.3847/1538-4357/ab3d33)
- CASA Team, Bean, B., Bhatnagar, S., et al. 2022, *PASP*, 134, 114501, doi: [10.1088/1538-3873/ac9642](https://doi.org/10.1088/1538-3873/ac9642)
- Casassus, S., Marino, S., Lyra, W., et al. 2019, *MNRAS*, 483, 3278, doi: [10.1093/mnras/sty3269](https://doi.org/10.1093/mnras/sty3269)
- Cazzoletti, P., Manara, C. F., Liu, H. B., et al. 2019, *A&A*, 626, A11, doi: [10.1051/0004-6361/201935273](https://doi.org/10.1051/0004-6361/201935273)
- Chung, C.-Y., Andrews, S. M., Gurwell, M. A., et al. 2024, *ApJS*, 273, 29, doi: [10.3847/1538-4365/ad528b](https://doi.org/10.3847/1538-4365/ad528b)
- Cieza, L. A., Ruíz-Rodríguez, D., Hales, A., et al. 2019, *MNRAS*, 482, 698, doi: [10.1093/mnras/sty2653](https://doi.org/10.1093/mnras/sty2653)
- Cieza, L. A., González-Ruilova, C., Hales, A. S., et al. 2021, *MNRAS*, 501, 2934, doi: [10.1093/mnras/staa3787](https://doi.org/10.1093/mnras/staa3787)
- Coutens, A., Liu, H. B., Jiménez-Serra, I., et al. 2019, *A&A*, 631, A58, doi: [10.1051/0004-6361/201935340](https://doi.org/10.1051/0004-6361/201935340)
- Delussu, L., Birnstiel, T., Miotello, A., et al. 2024, *A&A*, 688, A81, doi: [10.1051/0004-6361/202450328](https://doi.org/10.1051/0004-6361/202450328)
- Dent, W. R. F., Pinte, C., Cortes, P. C., et al. 2019, *MNRAS*, 482, L29, doi: [10.1093/mnras/lsy181](https://doi.org/10.1093/mnras/lsy181)
- Di Francesco, J., Johnstone, D., Matthews, B. C., et al. 2013, arXiv e-prints, arXiv:1310.1604, doi: [10.48550/arXiv.1310.1604](https://doi.org/10.48550/arXiv.1310.1604)
- Doi, K., Kataoka, A., Liu, H. B., et al. 2024, arXiv e-prints, arXiv:2408.09216, doi: [10.48550/arXiv.2408.09216](https://doi.org/10.48550/arXiv.2408.09216)
- Draine, B. T. 2006, *ApJ*, 636, 1114, doi: [10.1086/498130](https://doi.org/10.1086/498130)
- Dzib, S. A., Loinard, L., Rodríguez, L. F., et al. 2015, *ApJ*, 801, 91, doi: [10.1088/0004-637X/801/2/91](https://doi.org/10.1088/0004-637X/801/2/91)
- Foreman-Mackey, D., Hogg, D. W., Lang, D., & Goodman, J. 2013, *PASP*, 125, 306, doi: [10.1086/670067](https://doi.org/10.1086/670067)
- Francis, L., & van der Marel, N. 2020, *ApJ*, 892, 111, doi: [10.3847/1538-4357/ab7b63](https://doi.org/10.3847/1538-4357/ab7b63)
- Garufi, A., Carrasco-Gonzalez, C., Macias, E., et al. 2025, arXiv e-prints, arXiv:2501.11686, doi: [10.48550/arXiv.2501.11686](https://doi.org/10.48550/arXiv.2501.11686)
- Greaves, J. S., & Mason, B. 2022, *MNRAS*, 513, 3180, doi: [10.1093/mnras/stac856](https://doi.org/10.1093/mnras/stac856)
- Güdel, M. 2002, *ARA&A*, 40, 217, doi: [10.1146/annurev.astro.40.060401.093806](https://doi.org/10.1146/annurev.astro.40.060401.093806)
- Guidi, G., Isella, A., Testi, L., et al. 2022, *A&A*, 664, A137, doi: [10.1051/0004-6361/202142303](https://doi.org/10.1051/0004-6361/202142303)
- Guilloteau, S., Dutrey, A., Piétu, V., & Boehler, Y. 2011, *A&A*, 529, A105, doi: [10.1051/0004-6361/201015209](https://doi.org/10.1051/0004-6361/201015209)
- Han, I., Kwon, W., Aso, Y., Bae, J., & Sheehan, P. 2023, *ApJ*, 956, 9, doi: [10.3847/1538-4357/acf853](https://doi.org/10.3847/1538-4357/acf853)
- Hashimoto, J., Liu, H. B., Dong, R., et al. 2023, *AJ*, 166, 186, doi: [10.3847/1538-3881/acf3e9](https://doi.org/10.3847/1538-3881/acf3e9)
- Hashimoto, J., Muto, T., Dong, R., et al. 2021, *ApJ*, 911, 5, doi: [10.3847/1538-4357/abe59f](https://doi.org/10.3847/1538-4357/abe59f)
- Hildebrand, R. H. 1983, *QJRAS*, 24, 267
- Hoang, T., Lan, N.-Q., Vinh, N.-A., & Kim, Y.-J. 2018, *ApJ*, 862, 116, doi: [10.3847/1538-4357/aaccf0](https://doi.org/10.3847/1538-4357/aaccf0)
- Houge, A., Macías, E., & Krijt, S. 2024, *MNRAS*, 527, 9668, doi: [10.1093/mnras/stad3758](https://doi.org/10.1093/mnras/stad3758)
- Huang, J., Andrews, S. M., Dullemond, C. P., et al. 2020, *ApJ*, 891, 48, doi: [10.3847/1538-4357/ab711e](https://doi.org/10.3847/1538-4357/ab711e)
- Hull, C. L. H., Yang, H., Li, Z.-Y., et al. 2018, *ApJ*, 860, 82, doi: [10.3847/1538-4357/aabfeb](https://doi.org/10.3847/1538-4357/aabfeb)
- Isella, A., Carpenter, J. M., & Sargent, A. I. 2010, *ApJ*, 714, 1746, doi: [10.1088/0004-637X/714/2/1746](https://doi.org/10.1088/0004-637X/714/2/1746)
- Isella, A., Chandler, C. J., Carpenter, J. M., Pérez, L. M., & Ricci, L. 2014, *ApJ*, 788, 129, doi: [10.1088/0004-637X/788/2/129](https://doi.org/10.1088/0004-637X/788/2/129)
- Kataoka, A., Muto, T., Momose, M., Tsukagoshi, T., & Dullemond, C. P. 2016a, *ApJ*, 820, 54, doi: [10.3847/0004-637X/820/1/54](https://doi.org/10.3847/0004-637X/820/1/54)
- Kataoka, A., Tsukagoshi, T., Momose, M., et al. 2016b, *ApJL*, 831, L12, doi: [10.3847/2041-8205/831/2/L12](https://doi.org/10.3847/2041-8205/831/2/L12)
- Li, Y.-P., Li, H., Li, S., et al. 2020, *ApJL*, 892, L19, doi: [10.3847/2041-8213/ab7fb2](https://doi.org/10.3847/2041-8213/ab7fb2)
- Liu, H. B. 2019, *ApJL*, 877, L22, doi: [10.3847/2041-8213/ab1f8e](https://doi.org/10.3847/2041-8213/ab1f8e)
- Liu, H. B., Casassus, S., Dong, R., et al. 2024a, *ApJ*, 972, 163, doi: [10.3847/1538-4357/ad5dab](https://doi.org/10.3847/1538-4357/ad5dab)
- Liu, H. B., Galván-Madrid, R., Forbrich, J., et al. 2014, *ApJ*, 780, 155, doi: [10.1088/0004-637X/780/2/155](https://doi.org/10.1088/0004-637X/780/2/155)
- Liu, H. B., Galván-Madrid, R., Vorobyov, E. I., et al. 2016, *ApJL*, 816, L29, doi: [10.3847/2041-8205/816/2/L29](https://doi.org/10.3847/2041-8205/816/2/L29)
- Liu, H. B., Tsai, A.-L., Chen, W. P., et al. 2021, *ApJ*, 923, 270, doi: [10.3847/1538-4357/ac31b9](https://doi.org/10.3847/1538-4357/ac31b9)
- Liu, H. B., Muto, T., Konishi, M., et al. 2024b, *A&A*, 685, A18, doi: [10.1051/0004-6361/202348896](https://doi.org/10.1051/0004-6361/202348896)
- Long, F., Pinilla, P., Herczeg, G. J., et al. 2018, *ApJ*, 869, 17, doi: [10.3847/1538-4357/aae8e1](https://doi.org/10.3847/1538-4357/aae8e1)
- Long, F., Herczeg, G. J., Harsono, D., et al. 2019, *ApJ*, 882, 49, doi: [10.3847/1538-4357/ab2d2d](https://doi.org/10.3847/1538-4357/ab2d2d)
- Long, F., Pinilla, P., Herczeg, G. J., et al. 2020, *ApJ*, 898, 36, doi: [10.3847/1538-4357/ab9a54](https://doi.org/10.3847/1538-4357/ab9a54)
- Long, F., Andrews, S. M., Zhang, S., et al. 2022, *ApJL*, 937, L1, doi: [10.3847/2041-8213/ac8b10](https://doi.org/10.3847/2041-8213/ac8b10)
- Pérez, L. M., Chandler, C. J., Isella, A., et al. 2015, *ApJ*, 813, 41, doi: [10.1088/0004-637X/813/1/41](https://doi.org/10.1088/0004-637X/813/1/41)
- Piétu, V., Dutrey, A., Guilloteau, S., Chapillon, E., & Pety, J. 2006, *A&A*, 460, L43, doi: [10.1051/0004-6361:20065968](https://doi.org/10.1051/0004-6361:20065968)
- Pinilla, P., Benisty, M., Birnstiel, T., et al. 2014, *A&A*, 564, A51, doi: [10.1051/0004-6361/201323322](https://doi.org/10.1051/0004-6361/201323322)
- Rau, U., & Cornwell, T. J. 2011, *A&A*, 532, A71, doi: [10.1051/0004-6361/201117104](https://doi.org/10.1051/0004-6361/201117104)
- Reynolds, S. P. 1986, *ApJ*, 304, 713, doi: [10.1086/164209](https://doi.org/10.1086/164209)
- Ricci, L., Testi, L., Natta, A., et al. 2010, *A&A*, 512, A15, doi: [10.1051/0004-6361/200913403](https://doi.org/10.1051/0004-6361/200913403)
- Ricci, L., Trotta, F., Testi, L., et al. 2012, *A&A*, 540, A6, doi: [10.1051/0004-6361/201118296](https://doi.org/10.1051/0004-6361/201118296)

- Rodmann, J., Henning, T., Chandler, C. J., Mundy, L. G., & Wilner, D. J. 2006, *A&A*, 446, 211, doi: [10.1051/0004-6361:20054038](https://doi.org/10.1051/0004-6361:20054038)
- Rodríguez, L. F., Zapata, L. A., Dzib, S. A., et al. 2014, *ApJL*, 793, L21, doi: [10.1088/2041-8205/793/1/L21](https://doi.org/10.1088/2041-8205/793/1/L21)
- Salter, D. M., Kóspál, Á., Getman, K. V., et al. 2010, *A&A*, 521, A32, doi: [10.1051/0004-6361/201015197](https://doi.org/10.1051/0004-6361/201015197)
- Stephens, I. W., Lin, Z.-Y. D., Fernández-López, M., et al. 2023, *Nature*, 623, 705, doi: [10.1038/s41586-023-06648-7](https://doi.org/10.1038/s41586-023-06648-7)
- Tazzari, M., Testi, L., Ercolano, B., et al. 2016, *A&A*, 588, A53, doi: [10.1051/0004-6361/201527423](https://doi.org/10.1051/0004-6361/201527423)
- Terada, Y., Liu, H. B., Mkrtchian, D., et al. 2023, *ApJ*, 953, 147, doi: [10.3847/1538-4357/acdedf](https://doi.org/10.3847/1538-4357/acdedf)
- Testi, L., Birnstiel, T., Ricci, L., et al. 2014, in *Protostars and Planets VI*, ed. H. Beuther, R. S. Klessen, C. P. Dullemond, & T. Henning, 339–361, doi: [10.2458/azu\\_uapress\\_9780816531240-ch015](https://doi.org/10.2458/azu_uapress_9780816531240-ch015)
- Tripathi, A., Andrews, S. M., Birnstiel, T., et al. 2018, *ApJ*, 861, 64, doi: [10.3847/1538-4357/aac5d6](https://doi.org/10.3847/1538-4357/aac5d6)
- Ueda, T., Kataoka, A., & Tsukagoshi, T. 2022, *ApJ*, 930, 56, doi: [10.3847/1538-4357/ac634d](https://doi.org/10.3847/1538-4357/ac634d)
- van der Marel, N., Matthews, B., Dong, R., Birnstiel, T., & Isella, A. 2018, in *Astronomical Society of the Pacific Conference Series*, Vol. 517, *Science with a Next Generation Very Large Array*, ed. E. Murphy, 199, doi: [10.48550/arXiv.1809.06403](https://doi.org/10.48550/arXiv.1809.06403)
- van der Walt, S., Colbert, S. C., & Varoquaux, G. 2011, *Computing in Science and Engineering*, 13, 22, doi: [10.1109/MCSE.2011.37](https://doi.org/10.1109/MCSE.2011.37)
- Wu, Y. 2024, *ApJ*, 970, 25, doi: [10.3847/1538-4357/ad5553](https://doi.org/10.3847/1538-4357/ad5553)
- Wu, Y., Liu, S.-F., Jiang, H., & Nayakshin, S. 2024, *ApJ*, 965, 110, doi: [10.3847/1538-4357/ad323b](https://doi.org/10.3847/1538-4357/ad323b)
- Yamaguchi, M., Muto, T., Tsukagoshi, T., et al. 2024, *PASJ*, 76, 437, doi: [10.1093/pasj/psae022](https://doi.org/10.1093/pasj/psae022)
- Youdin, A. N., & Goodman, J. 2005, *ApJ*, 620, 459, doi: [10.1086/426895](https://doi.org/10.1086/426895)
- Zapata, L. A., Rodríguez, L. F., & Palau, A. 2017, *ApJ*, 834, 138, doi: [10.3847/1538-4357/834/2/138](https://doi.org/10.3847/1538-4357/834/2/138)
- Zhu, Z., Zhang, S., Jiang, Y.-F., et al. 2019, *ApJL*, 877, L18, doi: [10.3847/2041-8213/ab1f8c](https://doi.org/10.3847/2041-8213/ab1f8c)

## APPENDIX

## A. SPECTRUM CHARACTERIZATION

When the observations do not sufficiently constrain physical functions, or when the target sources are not yet well understood to the level that can enable physical modeling, we can characterize the observations using functions that are not directly linked to physics. For example, when analyzing a spectrum with only 2 or 3 independent measurements in the frequency domain, we need to make the choice of

1. fitting a power-law (which does not necessarily have a physical meaning) with a spectral index and report it, or
2. fitting the spectrum of a presumed dust emission source, and report the free-parameters such as dust column density, dust size (or beta), temperature, and solid angle, etc.

In many cases (e.g., when we cannot resolve degeneracy), only the first option is possible. For example, when observing  $\alpha = 3.2$  in a spatially unresolved source with only 200 GHz and 300 GHz measurements, it is not clear whether the source is optically thick or thin, and thus it is hard to extract useful physical parameters.

In light of this, in this work, we adopted an approach similar to that of the aforementioned option 1, to systematically characterize the spectra observed at  $>20$  GHz. The emission in this frequency range is not entirely dominated by free-free or synchrotron emission and thus is less subject to time variability. The main purpose is to quantitatively, jointly constrain the  $\alpha$  at high and low frequencies, and a transitional frequency. Specifically, we fit piecewise functions using the following strategy:

Since emission at  $>200$ –400 GHz and at  $<50$  GHz likely have distinct origins (e.g., the bulk of disks and localized high-density dust substructures, etc), we first separately fit the spectral profile at  $\lesssim 50$  GHz and at 200–400 GHz by two power-law functions, which are expressed as:

$$P_{\text{mm}}(\nu) = F_{44 \text{ GHz}} \left( \frac{\nu}{44 \text{ GHz}} \right)^{\alpha_{\text{mm}}}, \quad (\text{A1})$$

$$P_{\text{submm}}(\nu) = F_{230 \text{ GHz}} \left( \frac{\nu}{230 \text{ GHz}} \right)^{\alpha_{\text{submm}}}, \quad (\text{A2})$$

where  $\nu$  is frequency in GHz units,  $F_{44 \text{ GHz}}$  and  $F_{230 \text{ GHz}}$  are flux densities at the 44 GHz and 230 GHz reference frequencies, and  $\alpha_{\text{mm}}$  and  $\alpha_{\text{submm}}$  are the power law indices in the frequency ranges  $\sim 20$ –50 GHz and at 200–400 GHz, respectively. The power-law indices provide indications to the properties of the dominant emission sources at these two frequency ranges.

We then use the sigmoid function to characterize the smooth transition between the two power laws in the 50–200

GHz frequency range

$$\sigma_{\omega,b}(\nu) = \frac{1}{1 + e^{-\omega\nu + b}} = \frac{1}{1 + e^{-\omega(\nu - b/\omega)}} \quad (\text{A3})$$

where  $\omega$  is the parameter that determines the steepness of the transition, and  $b$  is the parameter that shifts the transition region in the frequency domain. When the transition is steeper, the value of  $\omega$  is larger. The mean frequency of the transition region is given by  $b/\omega$ , which indicates the frequency that the dust emission in the bulk of the dusty disk is becoming optically thin.

Using this strategy, each 20–400 GHz spectrum is effectively described by

$$F(\nu) = (1 - \sigma_{\omega,b}(\nu)) P_{\text{mm}}(\nu) + \sigma_{\omega,b}(\nu) P_{\text{submm}}(\nu), \quad (\text{A4})$$

where the six free parameters to fit are  $F_{44 \text{ GHz}}$ ,  $F_{230 \text{ GHz}}$ ,  $\alpha_{\text{mm}}$ ,  $\alpha_{\text{submm}}$ ,  $b/\omega$  and  $\omega$ .

When fitting  $P_{\text{submm}}(\nu)$ , we utilized the data taken from the SMA 200–400 GHz survey (Chung et al. 2024). To determine  $P_{\text{mm}}(\nu)$ , we focused on the Q, Ka, and K band data that were either taken from our JVLA observations (Section 2.2) or from the Disk@EVLA observations (Section 2.3). Since our data base is not uniform, we classified the sources into the following cases and treated the fitting to each case slightly differently: (1) For the few sources that the high  $\alpha_{33-44 \text{ GHz}}$  values are indicative of optically thin dust emission, if their  $\alpha_{33-44 \text{ GHz}}$  is higher than  $\alpha_{21-33 \text{ GHz}}$  (Haro 6-37, DR Tau, DN Tau and IQ Tau), we fit  $P_{\text{mm}}(\nu)$  to the K and Ka band data taken from the Disk@EVLA observations, (2) For the sources that missed Q or K band detection (Haro 6-39 and DL Tau) we treated them as special cases and addressed their fitting individually, (3) the fittings of the two sources UY Aur and V836 Tau are treated individually as exceptional cases, since their spectral indices increase with frequency in the 50–200 GHz and  $\sim 100$ –200 GHz frequency ranges, respectively, (4) for the rest of the sources, which are the majority, we fit  $P_{\text{mm}}(\nu)$  to the Q and Ka band data taken from the Disk@EVLA or our new JVLA observations.

For many sources that the low ( $\lesssim 50$  GHz) and high ( $>200$  GHz) frequency range spectral indices are similar (e.g.,  $\sim 2$ ), one may wonder if the *vertical offset* in the spectra that requires the sigmoid function is a flux calibration problem. This is not very likely, as the vertical offset in the spectra will appear large if the flux densities are presented in linear scale instead of log scale. Taking the observations on DN Tau as an example (Figure 2), to fit the data with a single smooth power law would require that the combined radio and/or the millimeter systematic flux errors are roughly a factor of 6. This is unrealistically huge as compared to the typically considered 3%–5% errors in the radio band and  $\sim 10\%$  errors in the millimeter bands. Moreover, if it was a flux scale issue, it should affect all the targets in a similar way. However, there

is a wide variety of vertical offsets between the low and high frequency regimes, again much larger than one could expect from flux scale concerns.

The individually treated cases are discussed as follows.

*Haro 6-39*—It was not observed in the Disk@EVLA project and was not detected at Q band in our new JVLA observations. We did not find other useful flux density measurements at Q band. As a tentative compromise, we fit  $P_{\text{mm}}(\nu)$  to the Ka and X band data taken from our new JVLA observations.

*DL Tau*—In this source, the Ka and Q band emission with a high  $\alpha_{33-44 \text{ GHz}}$  value may trace the optically thin tail of the small dust emission in the bulk of the disk. This source was not detected at K band in the Disk@EVLA observations, and was not detected in our new JVLA X band observations. For the sake of using the same functional form in the fitting, we fit  $P_{\text{mm}}(\nu)$  to the Ka band data taken from the Disk@EVLA observations and the 7.5 GHz flux density measurement quoted from Dzib et al. (2015). In this case, the frequency of the transition region ( $b/\omega$ ) is constrained by the fitting, while the  $P_{\text{mm}}(\nu)$  does not have a physical meaning.

*UY Aur*—Its spectral index at 200–400 GHz is  $\alpha_{200-400\text{GHz}} = 1.91 \pm 0.23$ . Its spectral index becomes smaller than 1.91 in a region between  $\sim 50$  GHz and 200 GHz (Figure 2). The spectral index at 33–44 GHz is relatively high ( $\alpha_{33-44 \text{ GHz}} = 4.04 \pm 0.55$ ). The most probable explanation for these spectra features is that the emission at 50–400 GHz and at higher frequency trace the optically thick dust emission in the bulk of the disk, and the  $\sim 30$ –50 GHz emission trace the optically thin tail of the dust emission from the bulk of the disk. The low spectral index at  $\sim 50$ –400 GHz is the most likely explained by the effect of dust self-scattering with  $a_{\text{maz}} \lesssim 1$  mm (Liu 2019), while the  $\alpha_{33-44 \text{ GHz}}$  value is also consistent with  $a_{\text{maz}} < 1$  mm. Our intention is to describe the optically thick dust emission in the bulk of the disk with the power law function  $P_{\text{submm}}(\nu)$ . Therefore, for UY Aur, we fit  $P_{\text{submm}}(\nu)$  to both the SMA 200–400 GHz data (Chung et al. 2024) and the Q band data taken from the Disk@EVLA survey.

*V836 Tau*—Comparing the 102.5 GHz flux density reported by Ricci et al. (2012) with the SMA 200–400 GHz measurements (Chung et al. 2024) indicates that its spectral index is  $< 2.0$  at 100–200 GHz, which signifies optically thick dust emission in the bulk of the disk with  $a_{\text{max}} \lesssim 500 \mu\text{m}$ . For a reason similar to that in the case of UY Aur, we fit  $P_{\text{submm}}(\nu)$  to the SMA 200–400 GHz measurements (Chung et al. 2024) and the 102.5 GHz measurement (Ricci et al. 2012).

When fitting the 4–400 GHz spectral profile with Equation A4, we included some flux densities at  $\sim 100$  GHz quoted from previous work (Piétu et al. 2006; Isella et al. 2010; Ricci et al. 2010, 2012; Guilloteau et al. 2011; Pinilla et al. 2014; Rodríguez et al. 2014; Dzib et al. 2015; Pérez et al. 2015; Tripathi et al. 2018; Huang et al. 2020; Long et al.

2020; Ueda et al. 2022). These data points help constrain the steepness ( $\omega$ ) and the frequencies of the turning points ( $b/\omega$ ) in the sigmoid function (Equation A3). For Haro 6-37, DR Tau, DN Tau, IQ Tau and DL Tau, which we did not use the Q band data in the fittings of  $P_{\text{mm}}(\nu)$ , we also included the Q band data when fitting  $F(\nu)$  in the last step.

We fit the six free parameters in the piecewise functions using the Markov chain Monte Carlo (MCMC) method, employing the Python package `emcee`. When fitting  $P_{\text{mm}}(\nu)$  and  $P_{\text{submm}}(\nu)$ , we assumed uniform prior functions within the ranges of 0.0–0.2 Jy, 0.0–2.0 Jy, 1.0–5.0 and 1.0–5.0, for  $F_{44 \text{ GHz}}$ ,  $F_{230 \text{ GHz}}$ ,  $\alpha_{\text{mm}}$  and  $\alpha_{\text{submm}}$ , respectively. The initial values of  $F_{44 \text{ GHz}}$ ,  $F_{230 \text{ GHz}}$ ,  $\alpha_{\text{mm}}$  and  $\alpha_{\text{submm}}$  were set to be 0.02, 0.2, 4.0, 2.0, respectively. We extracted the best fit parameters from the results of the power law fittings and assumed them as fixed parameters when fitting  $F(\nu)$ . After fixing the two power law functions,  $P_{\text{mm}}(\nu)$  and  $P_{\text{submm}}(\nu)$ , there are two remaining free parameters,  $b/\omega$  and  $\ln(\omega)$ . The prior function of  $\ln(\omega)$ , is uniform in the range of  $-3.9$ –0. The upper limit of  $\omega$  defines the steepest transition which is close to the step function, and the lower limit defines the smoothest transition. We set the prior function of  $b/\omega$  to be uniform within  $f_{\text{mm}, \text{max}} - f_{\text{submm}, \text{min}}$ , where  $f_{\text{mm}, \text{max}}$  is the maximum frequency of the data used in  $P_{\text{mm}}(\nu)$  fitting (e.g. 44 GHz), and  $f_{\text{submm}, \text{min}}$  is the minimum frequency of the data used in  $P_{\text{submm}}(\nu)$  fitting (e.g. 200 GHz). The range were chosen to restrict  $b/\omega$  within  $f_{\text{mm}, \text{max}} - f_{\text{submm}, \text{min}}$ . The initial values of  $\ln(\omega)$  and  $b/\omega$  were set to be  $-3.0$  and 100.0, respectively. The best fit parameters are summarized in Table 5.

In some sources, the best fit  $P_{\text{mm}}(\nu)$  functions present consistency with the measurements at  $< 10$  GHz frequencies (e.g., RY Tau, CW Tau, AB Aur). Many sources (e.g., LkCa 15, UX Tau, GO Tau, UZ Tau) at  $< 10$  GHz frequencies, which may be attributed to free-free and/or synchrotron emission.

In some cases, our best fits appear like step functions, which is largely a presentation effect. This is because we defined the best fit as the 50% percentile of our MCMC sample, which happened to be the ones that have relatively high  $\omega$  value (e.g., the case of V710 Tau in Figure 4). As can be seen in Figure 4 and Table 5, the same SED can be equally well fit with a lower  $\omega$  value (i.e., smoother transition). For most of the sources, the sigmoid functions have modest steepness with  $\omega \sim 0.5$ –0.8 (e.g., BP Tau, CI Tau, etc), although the value of  $\omega$  are subject to large error bars in many cases (e.g., IP Tau, Haro 6-39, V710 Tau). The three sources, DL Tau, DR Tau, and UZ Tau, may have relatively small  $\omega$  values ( $< 0.1$ ). For sources that present relatively steep transitions, the bulk of the disks may have relatively uniform dust column densities and maximum grain sizes. Conversely, DL Tau, DR Tau, and UZ Tau may have non-uniform distributions of dust column densities and maximum grain sizes in the bulk of their disks, such that different surface regions transits from optically thick to optically thin at different frequencies. Characterizing or categorizing the steepness of the transition therefore

provides useful information about dust processing in the protoplanetary disks.